POLITECNICO
MILANO 1863

SCUOLA DI INGEGNERIA INDUSTRIALE
E DELL'INFORMAZIONE

Computational Fluid Dynamics Investigation over a Reconfigurable Blade Tip for Helicopter Rotors

Tesi di Laurea Magistrale in
Ingegneria Aeronautica

Author: **Francesco Cambria**

Student ID: 968525
Advisor: Prof. Giuseppe Quaranta
Academic Year: 2021-22

Abstract

This thesis aims to evaluate an accurate aerodynamic model for the study of a reconfigurable helicopter blade tip based on a dihedral angle variation. The phase of flight considered is hovering.

It is known that a negative dihedral angle (so called *anhedral angle*) can improve performance during hovering but causes increased noise during forward flight due to blade-vortex interactions. The objective is to evaluate the effectiveness of a passive actuation of the tip reconfiguration mechanism through aeroelastic loads. Computational Fluid Dynamics is used as a tool to analyze the blade in different configurations.

A previous study of a multi-body system with a simplified aerodynamic model was used to gather information about the blade orientation during flight, its inertial values and also as a base comparison to further extend the accuracy of the analysis.

After validating the CFD model, various simulations of the blade at different anhedral angles were carried out. Besides, the variation of the tip hinge skew angle was deeply studied in order to find a possible better configuration. The obtained results are promising and indicate the possibility of passive actuation for a collective pitch lower than the one required for hovering. This value can easily be achieved during forward flight, thus allowing the reduction of the anhedral angle and the tip reconfiguration.

Keywords: helicopter, morphing, CFD, anhedral, tip

Abstract in lingua italiana

Questa tesi si propone di valutare un modello aerodinamico accurato per lo studio dell'estremità di una pala di elicottero riconfigurabile basata su una variazione dell'angolo di diedro. La fase di volo considerata è l'hovering.

È noto che un angolo di diedro negativo (*anedro*) migliori le prestazioni durante l'hovering, ma sia causa di una maggiorazione del rumore per la presenza dell'interazione pala-vortice (*blade-vortex interaction*). L'obiettivo è quello di valutare l'efficacia di un'attuazione passiva tramite i carichi aeroelastici del meccanismo di riconfigurazione dell'estremità della pala. La fluidodinamica computazionale viene utilizzata come strumento per analizzare la pala in diverse configurazioni.

Uno studio precedente di un sistema multicorpo con modello aerodinamico semplificato è stato utilizzato per raccogliere informazioni sull'orientamento della pala durante il volo, sui suoi valori inerziali e anche come base di confronto per estendere ulteriormente l'accuratezza dell'analisi.

Dopo la validazione della mesh e delle condizioni al contorno di CFD, si è passati alla simulazione della pala a diversi angoli di diedro e al confronto con i risultati precedentemente ottenuti dal sistema multicorpo. Lo studio si è focalizzato anche sull'orientamento dell'asse della cerniera dell'estremità. I risultati ottenuti sono promettenti e indicano la possibilità di attuazione passiva per passi collettivi inferiori a quello necessario per l'hovering. Questi valori possono essere raggiunti durante il volo avanzato, permettendo così la riduzione dell'angolo di anedro e la riconfigurazione dell'estremità della pala.

Parole chiave: elicottero, morphing, CFD, diedro, tip

Acknowledgements

First of all, I want to thank my parents who have loved, guided and pushed me ever since childhood to achieve my goals and commit to them. It is thanks to them that I am here today and have become the person I am. I will be forever grateful to them.

This thesis originated from a proposal by Professor Giuseppe Quaranta, my supervisor. I want to thank him for this opportunity and for helping me in the development of this project and in the completion of my studies.

Thanks to Clara, who has been with me throughout this journey and beyond. I could not have made it without her love and support in the many times of discouragement I have gone through. She always helped me find the positive side out of every situation, as only she is able to.

Thanks to Julien, my best friend and amazing partner in both adventures and study. The strength we gave each other every single day from the very start of the first year allowed us to get to the end of this together and in the best way possible. I would never have faced this path the same way without him.

And last but not least, thanks to everyone else. To the friends who have been there on this journey. To the buddies of university projects, mountain treks, skiing trips, and even epic sailing adventures. There have been times of joy and times of sorrow, but in the end I can say that I had a lot of fun, and what matters is remembering one's worth every day. And to never give up.

Contents

List of Figures

List of Tables

List of Symbols

Variable	Description	SI unit
$\boldsymbol{\mu}$	advance ratio	
$\boldsymbol{c}$	airfoil chord	m
$\boldsymbol{\beta_{tip}}$	anhedral angle	rad
$\boldsymbol{\alpha}$	angle of attack	rad
$\boldsymbol{p}$	apparent order method	
$\boldsymbol{R}$	blade radius	m
$\boldsymbol{\Gamma}$	circulation	m^2/s
$\boldsymbol{\theta_{75}}$	collective pitch angle	rad
$\boldsymbol{\beta_0}$	coning angle	rad
$\boldsymbol{\rho}$	density	kg/m^3
FM	figure of merit	
$\boldsymbol{\beta}$	flapping angle	rad
$\boldsymbol{u}$	flow velocity	m/s
$\boldsymbol{\omega}$	flow vorticity	s^{-1}
$\boldsymbol{r}$	grid refinement ratio	
$\boldsymbol{V_\infty}$	helicopter movement velocity	m/s
$\boldsymbol{\zeta_{th}}$	hinge line skew angle	rad
$\boldsymbol{W_{ideal}}$	ideal work required	Nm
$\boldsymbol{k}$	induced velocity parameter	
$\boldsymbol{F_{in}}$	inertial force	N
$\boldsymbol{M_{in}}$	inertial moment	Nm
$\boldsymbol{h}$	mesh grid spacing	
$\boldsymbol{I_{CG}}$	moment of inertia	$Kg\ m^2$
$\boldsymbol{\theta_{75}^0}$	null tip moment angle	rad

Variable	Description	SI unit
$\boldsymbol{P}$	pressure	Pa
$\boldsymbol{C_P}$	pressure coefficient	
$\boldsymbol{C}$	pure couple	Nm
$\boldsymbol{\Omega}$	rotational velocity	rad/s
$\boldsymbol{A}$	rotor equivalent area	m^2
$\boldsymbol{a}$	speed of sound	m/s
$\boldsymbol{v_{iM}}$	theoretical hover rotor induced velocity	m/s
$\boldsymbol{T}$	thrust	N
$\boldsymbol{C_T}$	thrust coefficient	
$\boldsymbol{\psi}$	tip center of mass anhedral angle	rad
$\boldsymbol{R_{CG}}$	tip center of mass radius	m
$\boldsymbol{M_{tip}}$	tip mach number	
$\boldsymbol{Q}$	torque	Nm

Introduction

Figure 1: Bell 212 helicopter taking off in mountainous conditions. Powder snow lifted from the ground makes wingtip vortexes visible - Personal shot

Helicopters represent some of the most complex and efficient machines created by man. Nowadays, their hovering and vertical movement capabilities make them crucial assets in carrying out several operations. Activities range from medical emergencies, reaching otherwise inaccessible remote places, search and rescue missions to military and strategical operations and construction sites support.

The development of these machines has proven to be quite difficult because of the inherent complication of their operation. In addition, the need for significantly more advanced and lighter materials along with more powerful engines greatly delayed the introduction of helicopters compared to fixed-wing aircraft (Leishmann, 2000 [9]). Nevertheless, the rotary wing retains excellent merits that make it the only solution for accomplishing flight

missions in a variety of conditions.

These days, the technical complications that made helicopters uncertain and ineffective machines have been overcome. The use of composite materials and of new design techniques that are extremely precise and effective has made possible to achieve flight performances that were unimaginable at the beginning of the last century. However, the world is changing and priorities are changing along with it. The new goals of the aviation industry are focusing less and less on pure flight capabilities and much more on fuel efficiency and noise reduction.

The use of helicopters in densely populated areas has a great impact on the surrounding population because of the loud noise generated by the rotor, especially during the landing phases. Therefore, in recent years the study of blade geometry has focused on efficiency and reduction of the main cause of impulsive noise - the *blade-vortex interaction (BVI)*.

Along the history of rotary-wing applications, many different blade tip shapes have been considered. According to Brocklehurst and Barakos [5], there still is no common agreement on the best design for a helicopter blade tip. However, several studies conducted on anhedral angles showed that hover performances are generally increased with a downward tip deflection. Nonetheless, helicopters are complex machines that need to operate in a variety of flight conditions, and hovering is just one of them; it is known that the anhedral angle is not an optimal feature during forward flight as it increases the vortex-blade interaction effect and thus the rotor noise, besides generally reducing flight performances. Because of this, the idea of a reconfigurable blade tip is born.

The concept of being able to modify the shape of a wing depending on flight conditions (*morphing*) has been deeply investigated by both academia and industry in recent years but with very little effective application in new projects. The general complexity of the rotary-wing system makes the design of a morphing component extremely difficult, and companies are reluctant to implement new technologies without first testing their effectiveness at length. One of the main problems is the implementation of any form of actuator inside of a rotor blade that is subjected to tremendous cyclic loads and transonic speeds. The concept of a passive actuation through the aerodynamic loads avoids the complication of large and bulky components and seems much more viable to adopt effectively. These days, the use of modern technologies like *Computational Fluid Dynamics (CFD)* and structural analysis software allow to elaborate accurate predictions of the rotor's performance and thus pave the way for more complex and precise analyses.

Objective

The purpose of this thesis is to evaluate the feasibility of a passive helicopter blade tip reconfiguration. The tip should be able to reduce the anhedral angle autonomously thanks to the loads generated in specific flight conditions. This way, the helicopter could switch from a hovering optimized configuration to a forward flight one (with little to no anhedral). The motion is made possible by the placement of a hinge at the start of the tip region, separating it from the inboard section of the blade, which remains undeformed.

This study is based on a preliminary examination of the problem made by J. Surra [20]. In that thesis, a multi-body model with simplified aerodynamics was build in order to analyze the blade. Both hovering and forward flight were deeply studied.

Taking part of the data from Surra's work as base information, this thesis dives further into the problem by implementing a Computational Fluid Dynamics model. This new aerodynamic approach will deliver more accurate results compared to the simplified theory, including three-dimensional effects that are missed by the simpler model. Once the setup is validated and the simulations run, results will be analyzed and compared to better understand the aerodynamic behaviour of the blade tip and evaluate if and at what conditions the anhedral reduction is possible.

Outline

This thesis is organized in five chapters

Chapter 1: problem definition concentrates on a general overview of the thesis environment. The rotor hovering flight is introduced, along with a summary of the tip shapes and their behaviour. After that, the previous work from Surra is presented with its techniques and results. Eventually, a brief explanation of CFD and the chosen method for the simulations are described.

Chapter 2: cfd model validation presents the Caradonna-Tung NASA experiment used as a reference for the validation of the CFD simulation of a rotor in hover. A particular focus on boundary conditions and meshing is depicted along with validation results. A deep mesh convergence analysis is provided for choosing the right setup for the simulations.

Chapter 3: helicopter blade introduces the reference blade used for the analysis and its geometry. All characteristics including geometric angles and inertial values are carefully reported. At the end, the CFD setting of the blade is presented.

Chapter 4: results displays the data gathered from CFD simulations of the blade in various configurations. First, results are compared with the previous multi-body study in the reference case. Then, a set of anhedral angles and blade hinge line orientations are investigated to understand the behaviour of the tip moments and the feasibility of passive actuation. Eventually. best tip configurations are found and discussed.

Chapter 5: conclusions and future developments presents the outcome of the study and summarizes the achieved results. Recommendations for future work and improvements of the model are also presented.

1 | Problem definition

In order to understand the scope of this study, it is necessary to introduce various physical and analytical concepts that are part of the problem. Information about current technologies and tools needed for the analysis is also provided. The aerodynamics of a helicopter rotor is an extremely complex topic; the flowfield is characterized by strong three-dimensional effects, unsteadiness and the constant interaction between the main helicopter components and the rotor wake.

1.1. Blade tip shapes

Modern helicopter blade tips are often modified with a combination of sweep and a negative dihedral angle (anhedral). For this study, the blade is rectangular and non-tapered.

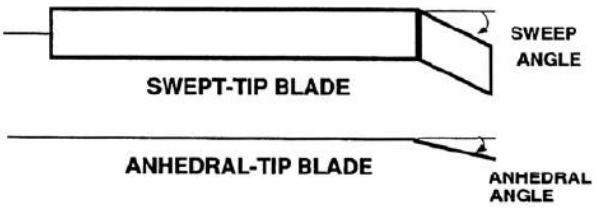

Figure 1.1: Tip shapes defined by Kim and Chopra (Barakos, 2013 [5])

The sweep angle moves the tip backwards and is needed for high speed reaching blades. The swept tip increases efficiency at high mach numbers by avoiding the delocalization of shock waves that could create peak loads and increase drag. The sweep angle also has a positive effect on advancing blades in forward flight.

However, the main drawback of this configuration is the translation of the tip's center of mass further back, away from the aerodynamic center line; strong aeroelastic effects due to pitching moments are generated by this change. In fact, the compressibility effects often require excessive sweep angles that are not achievable during design. Because of this, very thin airfoils are used on the blade tips, resulting in structural issues when the rotor undergoes heavy loading (Barakos, 2013 [5]).

The addition of the anhedral angle alleviates the problems caused by the sweep; the tip is moved downward out of the plane of the blade. Drooped and swept blades have

successfully been implemented on various projects, starting from the *British Experimental Rotor Programme (BERP)* (figure 1.2); this blade tip also presents a notch that tries to solve the CG retreat problem by shifting it forward and allowing higher sweep angles. The anhedral angle is also present on propeller blades to improve efficiency. Muller and Staufenbiel [16] investigated the aerodynamic performance of rotors with anhedral blade tips, and the results showed that the rotor hover performance increased. A very small increment of the forward flight figure of merit is also acknowledged, specifically on low aspect ratio blades (Barakos, 2013 [5]). The anhedral angle will be deeply investigated in this study to show its positive effects on the hovering flight.

Figure 1.2: BERP blade tip (Marques, 2013 [15])

1.2. Hovering flight

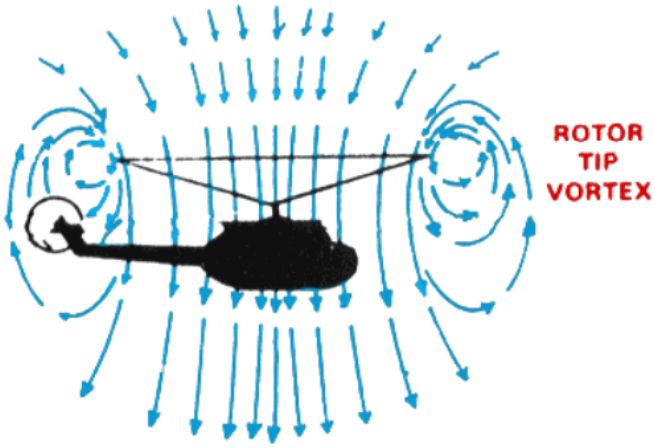

Figure 1.3: Hovering flow depiction

Hovering is the most basic flight condition for a rotary-wing aircraft. The goal of the rotor is to sustain the gross weight of the helicopter, keeping the machine airborne with no horizontal or vertical movement. Each blade is subject to a constant rotational velocity

along the whole path around the rotor disc. With the formula

$$v(r) = \Omega \cdot r = v_{tip}\frac{r}{R} \tag{1.1}$$

the tangential velocity profile on the blades is depicted. As it linearly increases towards the tip, the outer portion of the blade is the one subject to the strongest loads.

A rotor generates a vertical thrust T and a resistance torque Q. With these components it is possible to define the two main coefficients.

$$C_T = \frac{T}{\rho A(\Omega R)^2} \tag{1.2}$$

$$C_Q = \frac{Q}{\rho AR(\Omega R)^2} \tag{1.3}$$

These two equations represent respectively the thrust coefficient C_T and the torque coefficient C_Q.

In order to generate the thrust required for hovering, the blades are inclined of a pitch angle θ imposed by the pilot. As the rotor spins and the pressure distribution arises, it is known that a three-dimensional wing will produce a *downwash* flux of air that takes part in the induced drag generation. The representation of figure 1.3 gives an idea of the vertical motion of air through the rotor disc during hover. This induced vertical velocity modifies the relative angle between the blade section and the relative air flow, actually reducing the effective angle of attack α. This translates in lowering the generated lift and thus an even higher pitch angle is required to sustain the helicopter's weight. Overall, the rotor generates less thrust and more drag in reality if compared to an hypothetical environment with no vertical inflow.

Therefore, the induced velocity must be considered in a model that reproduces the hover flight. The *momentum theory* is a useful and simple tool that can be used to compute its value. With the actuator disk assumption, the formula

$$v_{iM} = \sqrt{\frac{T}{2\rho A}} \tag{1.4}$$

delivers the value of the induced velocity just above the rotor surface.

From the elements previously described, one can compute the hover figure of merit; detailed description of the process is reported in Leishman (2006, [9]). It is defined as the ratio between the ideal power from momentum theory and the actual power required by

the rotor.

$$\mathrm{FM} = \frac{W_{ideal}}{W} = \frac{T\ v_{iM}}{Q\ \Omega} = \frac{T\ \sqrt{\frac{T}{2\rho A}}}{Q\ \Omega} \tag{1.5}$$

Many studies confirm that the presence of an anhedral angle on the blade tip improves the efficiency of the hovering. According to Shuilin (2018) [6] and Uluocak (2021) [19], the anhedral significantly reduces the intensity of the wingtip vortexes. Another consequence is a smaller overall thrust, but this is largely compensated by the gain in drag reduction from the smaller vortexes and thus translates to a higher figure of merit. Besides, the vortexes are generated away from the rotor plane and tend to move radially closer to the center.

1.3. Blade Vortex Interaction

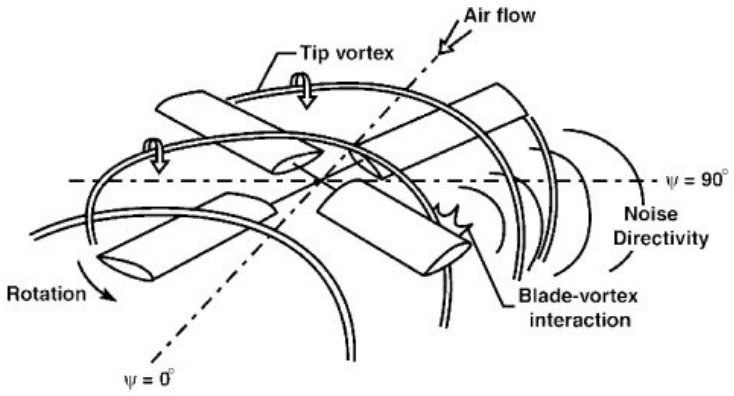

Figure 1.4: Schematic representation of blade-vortex interactions

Understanding the different sources that produce the rotor noise is still very difficult due to the complexity of the flow field of a rotary-wing system. Among the others, impulsive noise generated by blade-vortex interaction is certainly the dominant sound contributor and one of the major limitations of helicopter operations in urban areas. For these reasons, it is the cause of many unused heliports around the world. Therefore, considering the noise restrictions imposed by govern-

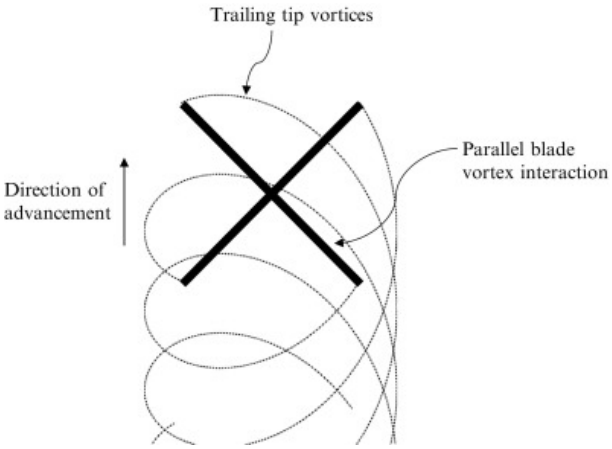

Figure 1.5: BVI in forward flight (Glegg, 2017 [18])

ments and ICAO, the aeroacoustic behaviour of rotors must be taken into account.

The blade-vortex interaction is an aerodynamic phenomenon that consists in a sudden pressure variation on the leading edge of a blade due to the contact with a vortex previously shed by another blade of the rotor. This effect is mostly present in forward flight, when the wake of the advancing blades is hit by the retreating blades in a epicyclic shape. This causes a characteristic *blade slap* sound that is particularly intense in manoeuvres, descent and landing. Besides the generated noise, strong vibrations also occur and are perceived by passengers inside the helicopter; these vibrations can also damage the structure and produce fatigue loads (Glegg, 2017 [18]).

For specific forward flight trim conditions, the vortex-blade interaction is enhanced by the presence of the anhedral angle on the blade tip. Also, as stated by Hollands, Keßler and Kräme [10], the loss in figure of merit during forward flight of an anhedral blade is greater than the figure of merit gain during hover; in fact, a dihedral angle (positive) would be preferential in this condition. Consequently, a reconfigurable system that nullifies the anhedral once in forward flight is desirable.

1.4. Tip reconfiguration mechanism

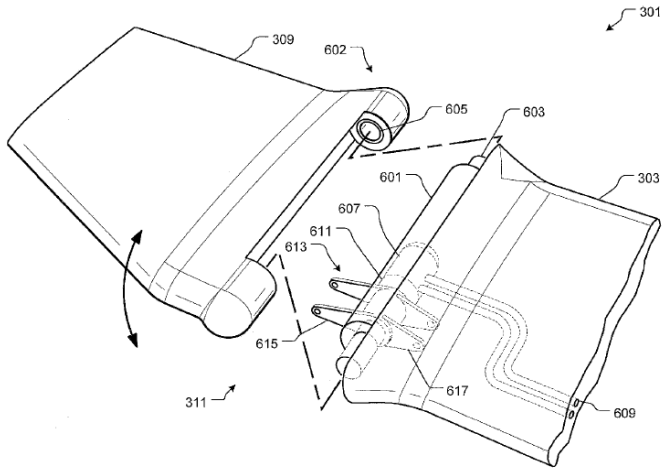

Figure 1.6: Patent of a the reconfigurable tip system (Foskey, 2016 [2])

One of the main problems of geometry variation in rotor blades is the implementation of an effective actuator system that does not interfere with regular operations of the helicopter. The heavy loading and inertia forces of a rotating blade make this task extremely challenging. For these reasons, very few applications have been developed in recent years. The one by Foskey [2] is the only registered patent that was specifically developed for

rotor blade tips.

The system presents a cylindrical hinge composed of some pins and a hydraulic actuator. This configuration allows for a linear deflection of the blade tip up to 90° anhedral. No detail is given on how the hydraulic system should be implemented inside of the blade, but the author states clearly that this design could be exploited in a variety of ways, including electrical motors, that differ from the base configuration exposed in the patent. Besides, the influence of aerodynamic and inertia forces are cited multiple times, as they could be helpful in the movement of the tip by reducing the necessary power provided by the actuator.

The idea behind this thesis is to evaluate the viability of a setup that does not require an actuator of any kind; this would eliminate the implementation problem of it and have little to no impact in terms of weight or structure of the blade. The hinge would be equipped with a sprag wheel and a stopping mechanism, allowing a one-way-only rotation of the tip. This way, the extremity could rotate freely under the aerodynamic loads in the direction of anhedral reduction. The system could be released or blocked through the use of a button, such that the pilot could effectively change the anhedral angle of the blades depending on the flight conditions and on blade-vortex interaction perception.

The hinge could also be designed not as a separate component inside of the blade, but as a part of the structure with lower stiffness. If properly shaped with the use of composite materials, the blade could actually change its geometry in a non-linear way around a certain *hinge region* of its length.

1.5. Previous multi-body model analysis

The subject of this thesis was first studied by J. Surra (2019, [20]) through the implementation of a multi-body model of the entire rotor.

First, a Finite-Element model of the blade was built by assessing its internal structure, subdivided in skin, spar and core. A study of the appropriate materials based on composites was conducted. Mass and inertia values were extrapolated from this model built in Femap.

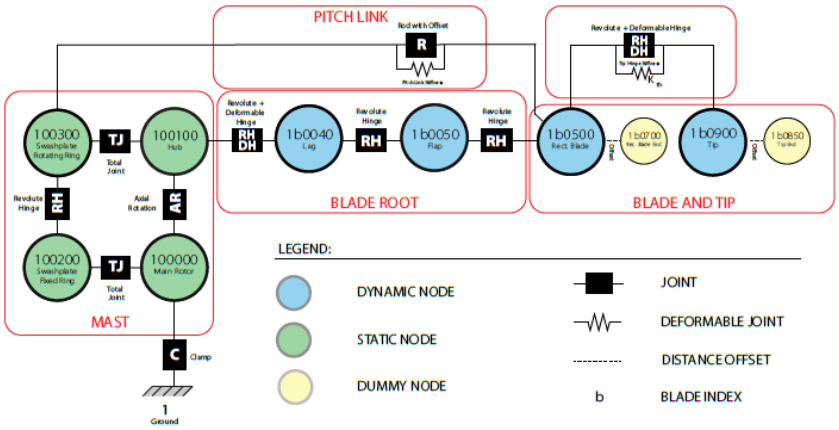

Figure 1.7: Conceptual representation of the full multi-body model (Surra, 2019 [20])

After focusing on the blade structure, the multi-body model was build by also taking into account the presence of the swashplate. A multi-body model is a system of mechanical elements that move by following set constraints (e.g. joints); these elements are chosen from a library and can be both flexible or rigid. The blade model is made of four sections: mast, blade root, blade, tip and the pitch link which connects the movement of the swashplate to the blade.

The blade tip is composed of several aerodynamic bi-dimensional panels that evaluate loads through the *Blade Element Momentum Theory (BEMT)*, a method usually adopted on propellers. It unites the blade element theory and the momentum theory to calculate the inflow on the blades; the solution is obtained by solving a system of nonlinear equations (Ledoux, 2021 [8]). Correction coefficients for tip and hub loss can be applied to the equations to simulate the presence of three-dimensional effects.

After various simulations and the evaluation of the tip sensitivity to anhedral and hinge angles, the study concluded that a moment sign change occurs at approximately 10° pitch angle in hovering. It would then be possible to set the pitch accordingly to a desired

reduction or increase of the anhedral angle. Little anhedral reduction was achieved in forward flight. However, as the author states *'...the application of CFD analyses proves necessary to predict the flowfield around the tip and...would permit a better estimation of the main players in the mechanism operations'.*

1.6. Computational Fluid Dynamics

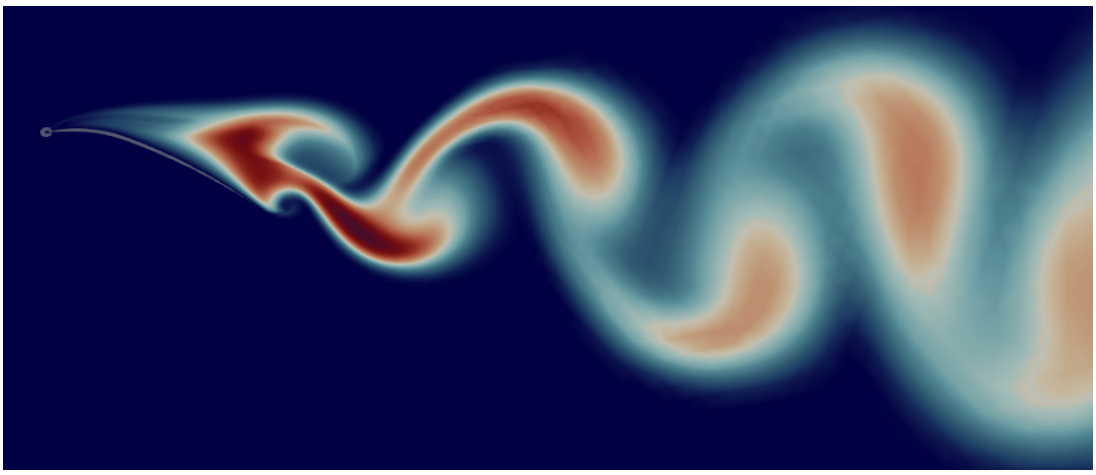

Figure 1.8: Eddy viscosity visualization of the Von Kármán street of a stalled airfoil - Personal image

'Computational fluid dynamics (CFD) is a science that, with the help of digital computers, produces quantitative predictions of fluid-flow phenomena based on the conservation laws (conservation of mass, momentum, and energy) governing fluid motion.' (Fluid Mechanics, 5th edition, 2012 [14])

The Navier-Stokes equations govern the dynamics of any fluid motion. They are highly non-linear and coupled equations that still lack a general analytical solution. Although they were formalized in the first half of the 19th century, they constitute one of the biggest challenges in the world of aerodynamics up to this day. Historically, experimentation in wind tunnels has always been the main way of analyzing a flow phenomenon, but can often be prohibitively expensive or impossible.

The birth and development of CFD has brought new light on a variety of problems and heavily accelerated the design process of many projects. A great example is the discovery of the *wall cycle* and of the small coherent structures of turbulence (*attached eddies*); these phenomenons were so small that it was impossible to identify them experimentally. They were found when supercomputers were powerful enough to solve *Direct Numerical*

Simulations (DNS) of very detailed wall regions. However, the computational expense of these methods still is one of the hardest problems for modern high performance computing. Simplified models of the Navier-Stokes equations were developed for specific cases that required less precision or were not influenced by certain effects.

A standard CFD simulation utilizes a Finite-Volume method; a certain domain of fluid is discretized in small volume cells along a pattern called *mesh* or grid. Inside of each cell, governing equations are solved iteratively and boundary conditions with neighbouring elements or walls apply. The unsteady nature of flow fields together with the complexity of the equations make computational instability one the lead problems in the world of CFD. In 1928, the *Courant-Friedrichs-Lewy condition (CFL)* was developed and it is still used today. The CFL states that information cannot flow across an entire cell during one iteration, thus the step has to be small enough to account for this effect (Abraham, 2021 [17]). Several parameters have to be carefully set in order to obtain good quality results from a simulation. The risk of delivering unrealistic data is very high, and that is why every CFD simulation still needs a validation study of its capabilities.

This thesis focuses on the analysis of a helicopter rotor in hover with the objective of evaluating loads generated by aerodynamic forces. Since the blades are constantly away from stall conditions and the rotor wake is not of primary concern, the inviscid Euler equations were chosen as the simulations' model. This allows the mesh to be coarser and the computation to be way less expensive compared to a RANS turbulent model.

$$\frac{\partial \rho}{\partial t} + \nabla \cdot (\rho \vec{u}) = 0 \tag{1.6}$$

$$\frac{\partial \rho \vec{u}}{\partial t} + \nabla \cdot (\rho \vec{u} \otimes \vec{u} + pI) = 0 \tag{1.7}$$

$$\frac{\partial E_{tot}}{\partial t} + \nabla \cdot [\vec{u}(E_{tot} + p)] = 0 \tag{1.8}$$

This set of equations need to be closed with a complete fluid model. In this case, the rotor blades spin at a speed that is high enough to make compressibility effects play a role. Therefore, the ideal gas law is applied and the equations are kept in the full, compressible form. Although rotating at high speed, the rotor is not in the shock wave generation range, thus there is no need to implement specific mesh refinements in this regard.

2 | CFD model validation

2.1. Experiment definition

In order to validate the CFD model, the Caradonna-Tung NASA experiment [4] was taken as a reference. Various simulations were performed on this setting and proven to be representative of true results.

The experiment consists of two NACA 0012 blades rotating at a constant speed. Characteristic values are reported in table 2.1.

The simple rectangular blades were mounted on a central mast and fixed to it through their aerodynamic center line at approximately 25% of the chord with a half degree precone. The rotors were placed at the center of a tall chamber equipped with special ducting to eliminate room recirculation. This configuration allowed to test the blades at different collective pitch angles and consequently, angles of attack; for this validation the case of 8° was mainly considered. The rotor is regarded as in a hovering condition.

A vast distribution of pressure taps was mounted on the blades in order to evaluate the pressure and thrust coefficients.

Blade Chord c	0.191 m
Blade Radius R	1.143 m
Aspect Ratio	1/6
Cut-out radius	0.191 m
Collective Pitch	8°
Rotational Speed Ω	1250 rpm
Experimental C_T	0.00459
Mach number at blade tip	0.439
Operative pressure P	103027 Pa

Table 2.1: Caradonna-Tung experiment setting values

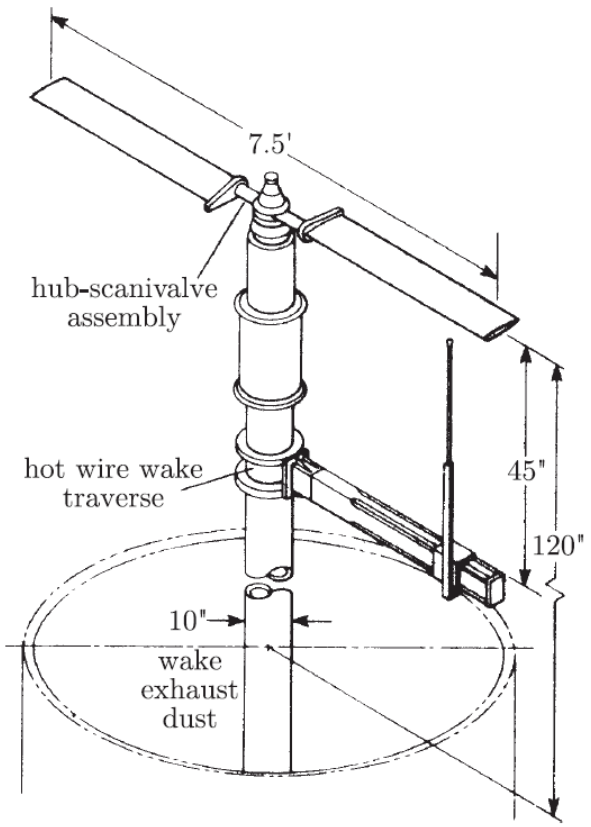

Figure 2.1: The Caradonna-Tung experiment

2.2. CFD simulation domain and settings

The validation consisted of two subsequent sets of CFD simulations. The first one with a large complete domain, and the second one with a much smaller, half-split periodic domain in order to reduce computational cost.

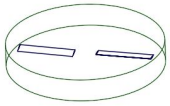

Figure 2.2: Blades' inner rotating domain

The first simulation included a cylindrical domain of radius 30 R and same height. The whole boundary was set as a pressure outlet with standard values. A smaller cylinder of radius 1.5 R was placed around the blades as the rotating domain.

The inner domain, depicted in figure 2.3, allowed for the application of the moving reference frame method, which delivers a stationary rotational flow around the rotor without the need of a moving mesh or time marching simulations.

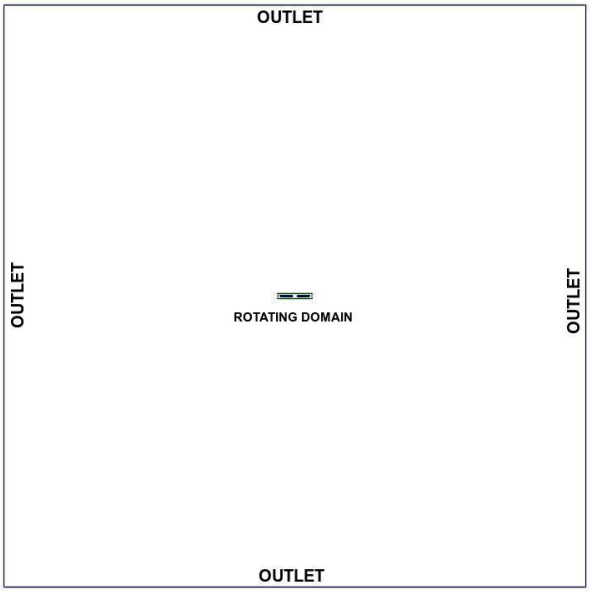

Figure 2.3: Caradonna-Tung CFD domain and boundary conditions

The discretization methods chosen were a second order upwind for the momentum equation and a second order for the continuity equation.

Considering the wing tip mach number, compressible conditions were met. The CFD solver includes the energy equation and the ideal gas law is set to use in the simulations.

The goal thrust of the rotor was evaluated through the experimental c_T, which formulation was already discussed in chapter 1.2. Thrust was extrapolated from the coefficient by using equation 1.2.

Pressure distributions at blade's sections were also taken from the available experimental data.

2.2.1. Moving Reference Frame

The simulations were performed by using a rotating reference frame; the inner domain was set to have the same rotation speed as the blades. This way, the continuity, momentum and energy equations are re-written in the moving reference frame by taking into account the rotational velocity on the subdomain.

Considering a coordinate system which is rotating steadily with angular velocity $\vec{\Omega}$ relative to a stationary (inertial) reference frame, every point inside the rotating subdomain is defined by a vector $\vec{r}$ from the origin of the relative reference frame. Therefore, the fluid velocities can be transformed from the stationary frame to the rotating frame using the

following relation:

$$\vec{v_r} = \vec{v} - \vec{u_r} \tag{2.1}$$

where

$$\vec{u_r} = \vec{\Omega} \times \vec{r} \tag{2.2}$$

In the equations, $\vec{v_r}$ is the relative velocity, $\vec{v}$ the absolute velocity and $\vec{u_r}$ is the velocity due to the motion of the rotating frame, known as *whirl* velocity.

With these new terms in mind, the governing Euler equations for a steadily rotating frame can be re-written as follows:

$$\frac{\partial \rho}{\partial t} + \nabla \cdot \rho \vec{v_r} = 0 \tag{2.3}$$

$$\frac{\partial \rho \vec{v}}{\partial t} + \nabla \cdot (\rho \vec{v_r} \vec{v}) + \rho(\Omega \times \vec{v}) = -\nabla p \tag{2.4}$$

$$\frac{\partial \rho E}{\partial t} + \nabla \cdot (\rho \vec{v_r} H + p \vec{u_r}) = k \nabla^2 T \tag{2.5}$$

In this new formulation, Coriolis and centripetal accelerations appear through the term $(\vec{\Omega} \times \vec{v})$ in the momentum equation and they deliver the steady state solution of a constant rotational velocity flow. This avoids the need of a time marching simulation and of a moving mesh, both extremely expensive in terms of computational power (Ansys Fluent Manual [3]).

2.2.2. Pressure-Velocity coupling

In order to obtain substantially faster convergence, Ansys Fluent uses an additional condition on pressure obtained through the discretization of the continuity equation. This *pressure-based* solver allows to solve the flow problem with a coupling between velocity and pressure, the so called COUPLED scheme.

As stated in Ansys Fluent manual [3] *"The coupled scheme obtains a robust and efficient single phase implementation for steady-state flows, with superior performance compared to the segregated solution schemes"*.

The continuity equation is re-written in a pressure-based version and solved together with the momentum equation, increasing convergence speed.

2.2.3. Meshing

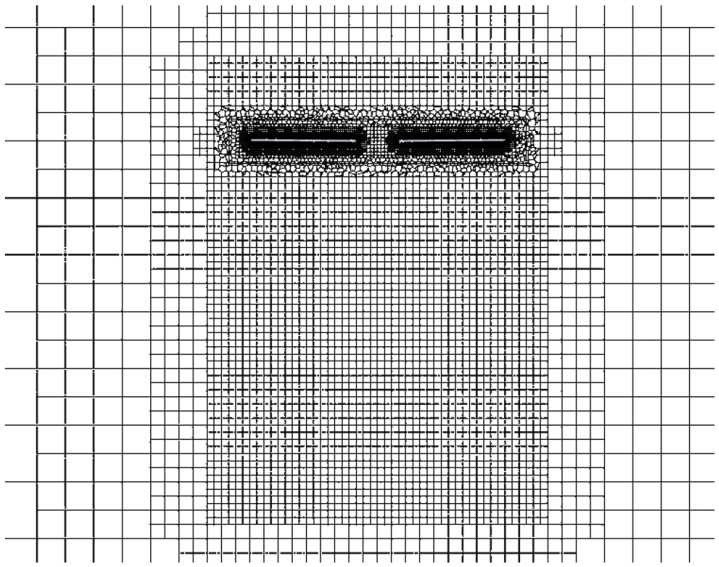

Figure 2.4: Front view of blades' mesh

The meshing of the full domain resulted in 4 million elements with a uniform refinement on the blade of 1 mm size. A finer region was created around the blades and the inner rotating domain, while keeping the outer cells larger. In figure 2.4 a mid section of the domain showing the mesh is represented. The blades are surrounded by a darker area, which signifies finer cells. The region expands downwards to better capture the wake close to the rotor and avoid loads oscillations.

Poly-exacore elements were preferred over classic tetrahedrons as they allow for a strongly smaller mesh while maintaining and actually increasing quality and robustness. These elements can speed up converge from 10% to 50% depending on the applications (Annual CFD Symposium 2019 [22]). Also, the higher number of faces per element compared to tetrahedrons is more indicated for rotor simulations; this way, the strongly varying flow direction is better captured and the numerical flux error is reduced.

The trailing edge of the blade required special care. In general, sharp and pointy models lead to low-quality meshes that can also generate errors and be impossible to use. Therefore, the solution was to cut the trailing edge by giving it a finite size; this is reasonably small in order to

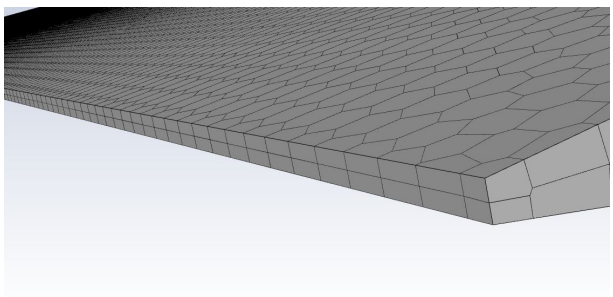

Figure 2.5: Particular of cut trailing edge mesh

not interfere with the physics of the problem. In this case, the trailing edge has a vertical dimension of 0.25% of the airfoil's chord. The proximity law on the trailing edge region created a mesh fitting two cells into the cut for better accuracy.

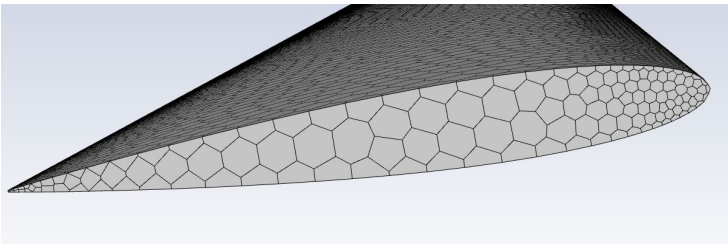

Figure 2.6: Particular of airfoil meshing curvature and proximity methods (*coarse* mesh)

On the split domain, a better educated mesh refinement was applied on the blade, concentrating finer areas on the leading edge and trailing edge locations; this meshing was done using curvature and proximity algorithms. After validating this setup compared to the full domain one, three meshes were built: a *coarse*, *medium* and *fine* mesh. Later, a mesh convergence study was performed.

2.2.4. Periodic conditions and domain splitting

After witnessing the accuracy of the first simulation with the experimental values, the domain was split in half introducing a periodic boundary condition on the inner sides, consequently reducing the elements number and the calculation effort.

The vertical dimensions were also lowered to 4 R on the top and 6 R on the bottom, as these dimensions guarantee to avoid boundary proximity effects (Doerffer, 2008 [13]). In this new configuration, an inlet velocity boundary condition has to be placed on top in order to simulate the induced velocity that the rotor naturally generates in a wider domain.

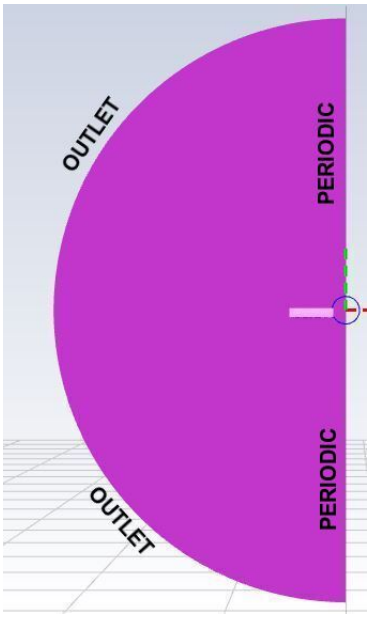

Figure 2.7: Split domain top view

As already seen in chapter 1.2, the hover induced velocity can be easily computed through the momentum theory using equation 1.4. Given the data from the Caradonna-Tung experiment and by using the thrust coefficient equation 1.2, the final value was $v_{iM} = 7.145$ m/s.

However, as the inlet is placed at a big distance from the blade to avoid boundary issues, the air further accelerates once close to the rotor and thus the thrust is excessively reduced compared to a true hovering case. Consequently, this primary formulation does not correctly represent the model.

In order to solve this problem, an experimental coefficient was computed such that:

$$v_i = k \cdot v_{iM} \tag{2.6}$$

An evaluation study of k was conducted in order to find the best value that equals the thrust given from the Caradonna-Tung experiment. Multiple simulations were performed with different inlet velocities based on k.

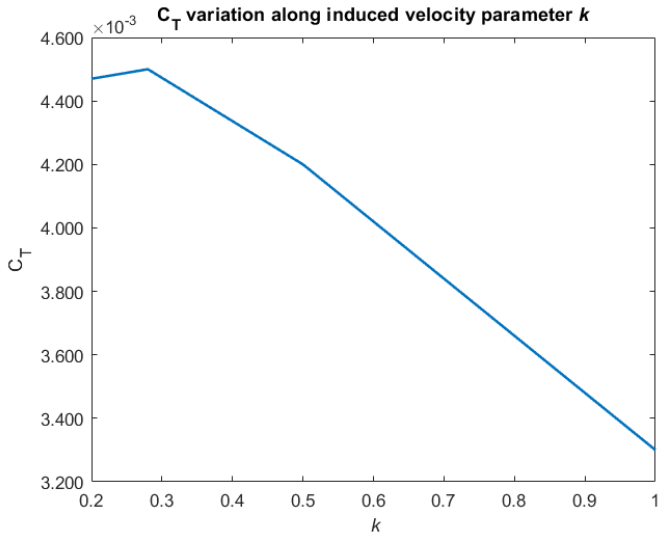

Figure 2.8: C_T versus experimental parameter k

The simulations' results are plotted in figure 2.8, trying to reach the thrust coefficient value computed experimentally by Caradonna and Tung. The final value of k used in the validation is 0.28. Lowering the inlet velocity any further reduces the quality of the solution and induces oscillations.

Being $k = 0.28$, the final inlet velocity results in a climbing rotor condition that equates the hover in terms of loads and pressure distribution. As a matter of fact, the actual induced velocity found on top of the blade matches with the theoretical one calculated through the momentum theory v_{iM}, as seen in figure 2.9. Clearly, the fictitious climb speed is the inlet velocity set on the boundary condition.

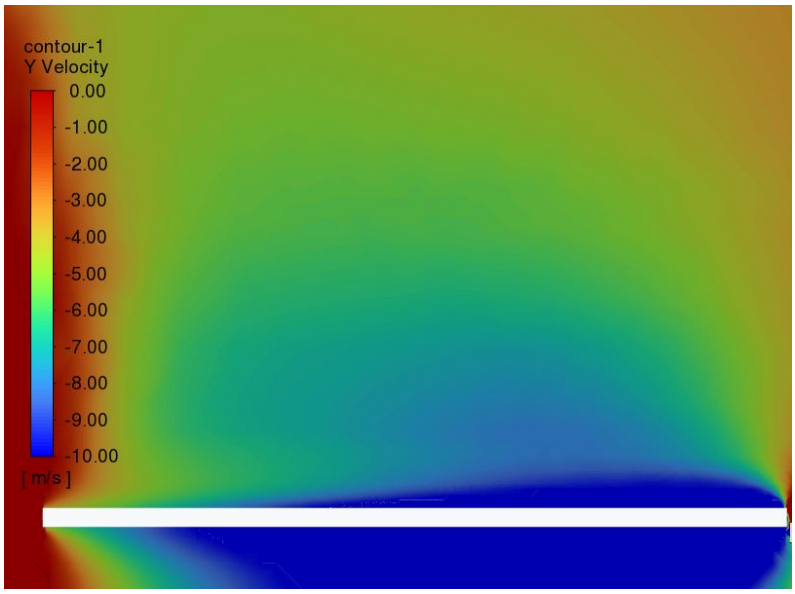

Figure 2.9: Vertical velocity distribution on top of the blade

2.3. Validation results

With an experimental thrust of 516 N, the full domain simulation delivered a result of 517 N.

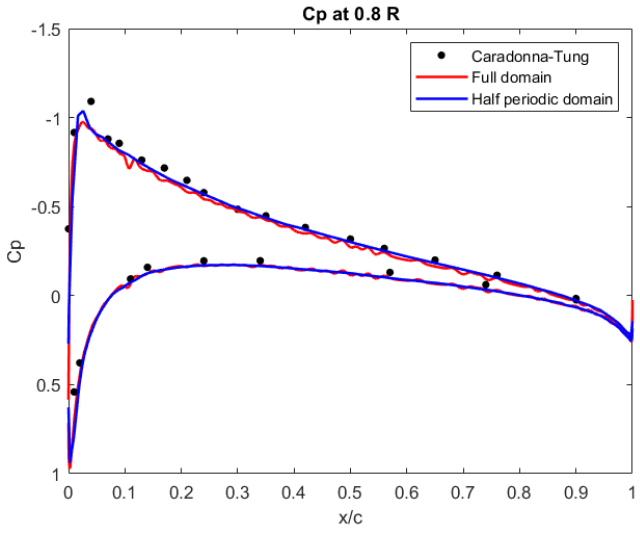

Figure 2.10: Pressure coefficient comparison at 80% radius section

At first, the 80% R section C_P was considered as a reference validation. There is no significant difference in results between the full domain with a much finer mesh and the half-split domain with the *medium* mesh.

The smaller domain-periodic boundaries simulation shows results that strongly relate both to the wide-domain simulation and the actual NACA experiment.

Once granted that the split domain with periodic boundaries delivers meaningful solutions, a mesh convergence study was performed with the use of a Richardson extrapolation over three meshes of different sizes. The procedure is done following the work by Meana-Fernández et al. (2019) [1].

The Richardson extrapolation method is used for obtaining a higher-order estimate of the theoretical value computed by an infinitely fine mesh (so called *zero grid spacing*). A numerical simulation yields a quantity that can be expressed as:

$$f = f_{exact} + g_1 h + g_2 h^2 + g_3 h^3 + ... \tag{2.7}$$

where h is the mesh grid spacing. Functions g_i are independent of h. f_{exact} is the continuum value at zero grid spacing.

By combining results f_1 and f_2 from two simulations with different grid spacing and by neglecting higher order terms (for a second order method), the zero grid spacing value may be computed as:

$$f_{exact} \approx f_1 + \frac{f_1 - f_2}{r^2 - 1} \tag{2.8}$$

where $r = \dfrac{h_{coarse}}{h_{fine}}$ is the grid refinement ratio.

This method can be generalized for a method of order p:

$$f_{exact} \approx f_1 + \frac{f_1 - f_2}{r^p - 1} \tag{2.9}$$

For this simulation, h was defined as a representative grid size parameter.

$$h = \sqrt{\frac{1}{N_S} \sum_{i=1}^{N_s} (\Delta V_i)} \tag{2.10}$$

where N_S is the number of cells and ΔV_i the single volume of a cell.

Considering the three meshes previously introduced, three different h are computed as well as two grid spacing ratios. From the three simulations come $r_{12} = 1.2205$ and $r_{23} = 1.1951$, both close to the recommended value of 1.3.

Mesh type	Elements number N_S	Grid spacing h	Computed thrust
coarse (3)	426738	0.0446	504.54 N
medium (2)	609491	0.0373	507.08 N
fine (1)	907853	0.0306	509.12 N

Table 2.2: Validation thrust results

The theoretical order of the simulation method is 2, but this value is different in the results due to numerical perturbation. Therefore, in order to find the apparent order of the method, the following equation is solved:

$$p = \frac{1}{ln(r_{21})}\left|ln\left|\frac{\epsilon_{32}}{\epsilon_{21}}\right| + ln\left(\frac{r_{21}^p - s}{r_{32}^p - s}\right)\right| \tag{2.11}$$

Where ϵ is the absolute error value between two simulations. Also, $s = \frac{\epsilon_{32}/\epsilon_{21}}{|\epsilon_{32}/\epsilon_{21}|}$. Clearly, equation 2.11 must be solved iteratively.

Eventually, the value of $p = 1.7571$ was found. The extrapolated value at zero grid spacing of the thrust can be found as:

$$T_{ext}^{21} = \frac{r_{21}^p T_1 - T_2}{r_{21}^p - 1} = 513.9865 \text{ N} \tag{2.12}$$

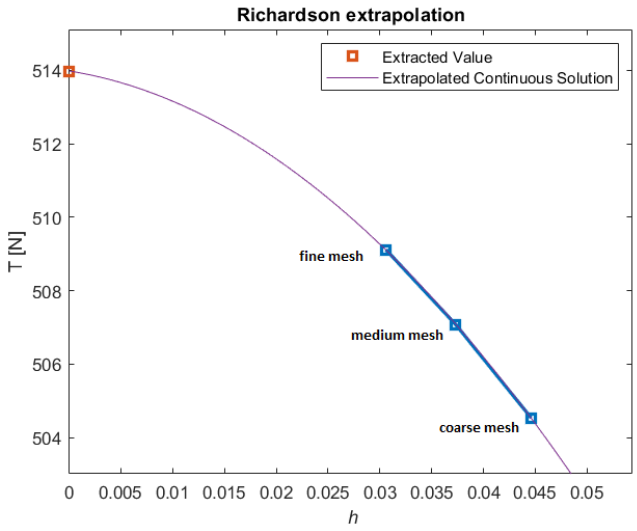

Figure 2.11: Grid convergence results

It is now possible to visualize the results. Figure 2.11 shows the three simulations and the extrapolated value at zero grid spacing. As expected, the order of the method is

almost perfectly quadratic. The grid convergence index (GCI) is used as an indicator of convergence level. It is defined as:

$$\mathrm{GCI}^{21} = \frac{F_S \, e_a^{21}}{r_{21}^p - 1} \tag{2.13}$$

Where e_a^{21} is the relative error between the two finer simulations and F_S is a security factor set at 1.25 when having three different meshes. For the two finer meshes, $\mathrm{CGI}^{21} = 1.194\%$.

The final value does not reach the experimental thrust of 516 N, and this will be investigated later. However, all meshes deliver an error that is less than 2.2% on the expected value. Because of this and due to computational costs, the settings of the *medium* mesh were chosen as reference for all further simulations in the thesis.

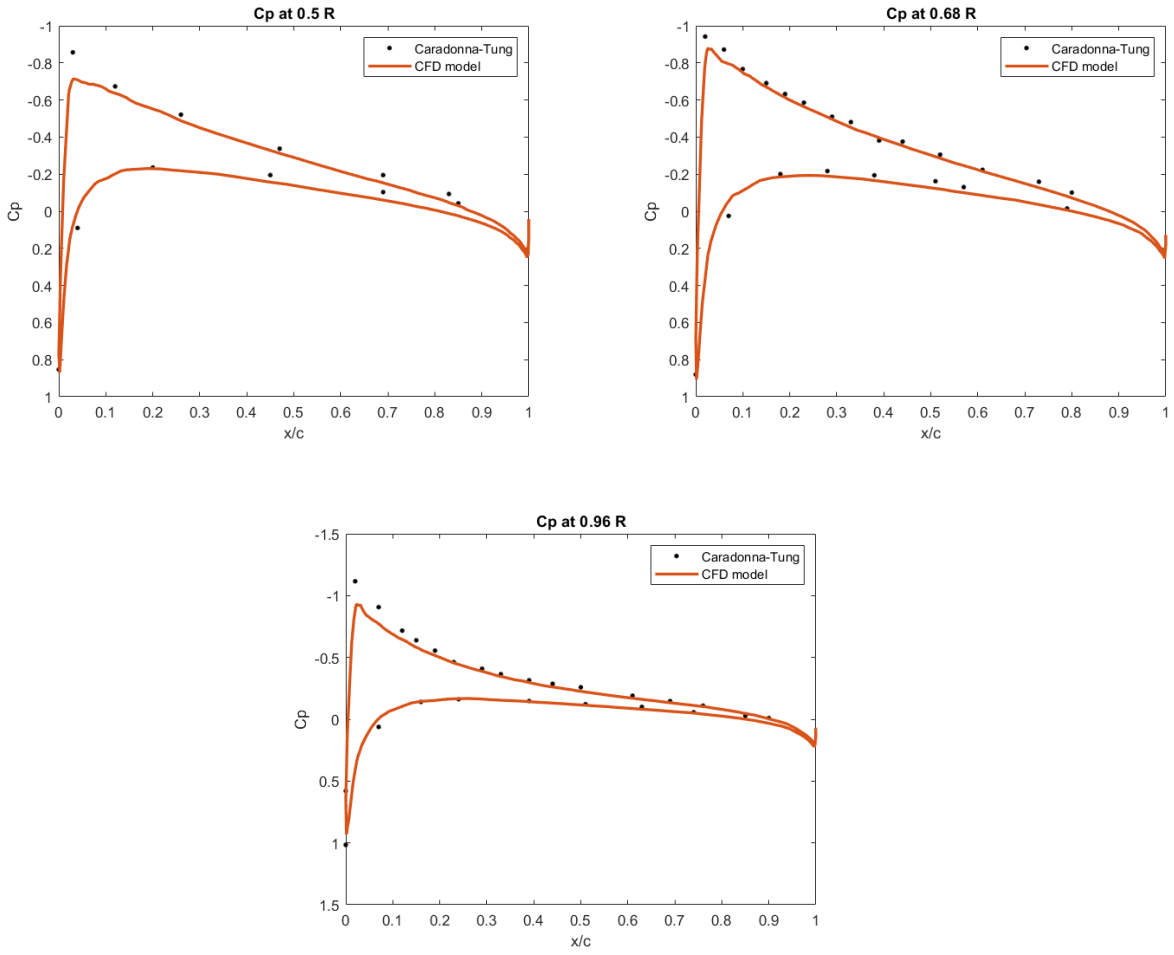

Figure 2.12: C_P evaluation at different blade sections

A further analysis of the pressure coefficient is conducted. In figure 2.12, graphs of the

C_P at 50%, 68% and 96% radius are plotted against the experimental values gathered from the pressure taps.

As can be easily assessed, the method presents a weak point in the evaluation of the suction peak on the nose of the airfoil, while the rest of the pressure coefficient distribution is faithfully represented. This is due to the use of the Euler equations and consequently of an inviscid simulation.

The use of a RANS model would deliver a representation of the boundary layer and the effects of viscosity. As it is well known, the boundary layer thickness interferes with the outer flow, and creates a further acceleration on the nose of the airfoil, eventually giving better results on the suction peak. This is the reason why the extrapolated value at zero grid spacing does not reach the experimental value completely.

This phenomenon was also witnessed by Morelli, Bellosta and Guardone [11] who performed a validation of the same experiment for the SU2 solver.

Nevertheless, considering the nature of this study, the error on the suction peak is considered to be negligible. The use of the Euler equations is justified by the regime condition and stationary aerodynamics of the problem; pressure integrals deliver accurate values of thrust compared to the experiment, which in fact is the crucial component in the evaluation of the blade's behaviour.

3 | Helicopter blade

3.1. Geometry

After having validated the CFD model, mesh and settings through the Caradonna-Tung experiment, it is possible to focus on the main objective of the thesis. Here, the reference helicopter blade and its geometry are introduced and described, with a specific attention to the rotor characteristics and the definition of inertial forces.

The study is focused on a 7.3 m long rectangular helicopter blade. The tip was then modified in order to account for both a sweep and anhedral angle β_{tip}. Unlike the previous multi-body study, the model will remain rigid in order to focus on the more accurate aerodynamic CFD analisys.

(a) Top view

(b) Front view

Figure 3.1: Blade 3D model rendered in SolidWorks

Figure 3.1 shows the final assembly of the reference helicopter blade. The blade's section is a NACA 23012 airfoil with a linear varying twisting angle along the span. This airfoil is one of the most common in the rotary-wing industry (Clay, Jacobs 1935 [21]). The

cut-out station is set to be at 10% R. The blade tip starts at 91% R, where its hinge is located. The tip also presents a fixed sweep angle of 25° and a reference anhedral angle β_{tip} of 20°.

Blade Chord c	0.327 m
Blade Radius R	7.3 m
Cut-out radius	0.191 m
Blade linear twist	-0.0213 rad/m
Blade cut-out twist	0.101 rad
Collective at 75% R	0 rad
Feathering axis position	0.23 c

Table 3.1: Blade characteristics

Using the values in table 3.2, the blade is built along the chosen feathering axis and the twist is distributed in order to obtain a null angle at 75% R. The linear twisting ends at the start of the tip, where the geometrical pitch angle drops to -0.118 rad, as seen in figure 3.4.

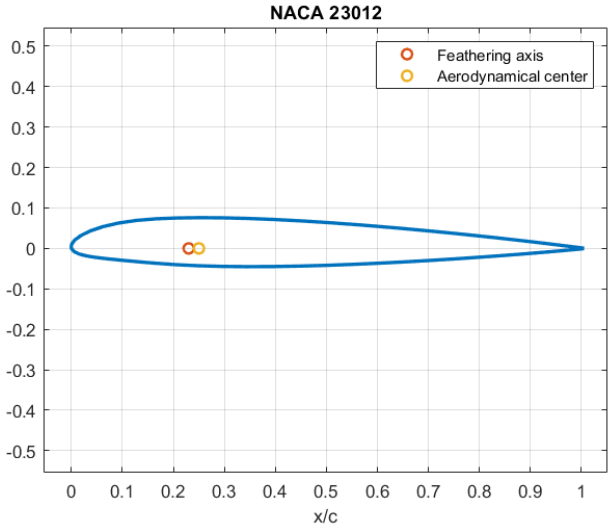

Figure 3.2: Blade section representation

Figure 3.2 represents the general blade section with the NACA 23012 airfoil. The feathering axis is set to be very close to the aerodynamic center (AC). The center of mass is positioned in front of the AC; this way, stability conditions are met. The trailing edge is cut in the same way as in the Caradonna-Tung experiment in order to facilitate the meshing process.

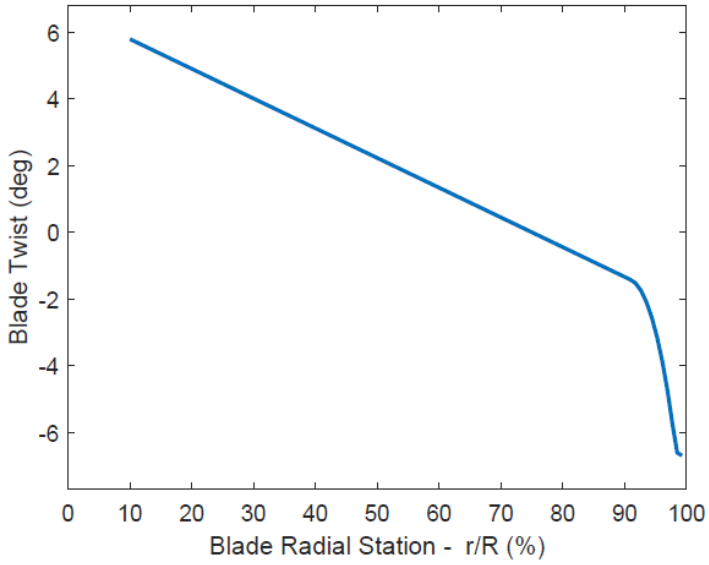

Figure 3.3: Blade twist

Figure 3.3 represents the twist angle distribution along the span, as previously described.

The twisting of the blade results in a variation of the geometrical angle of attack along the span; this follows the direction change of the speed vector, which becomes closer to parallel to the blade's chords by approaching the tip. This way, the true angle of attack remains constant along the whole blade and the stall of the tip region is avoided.

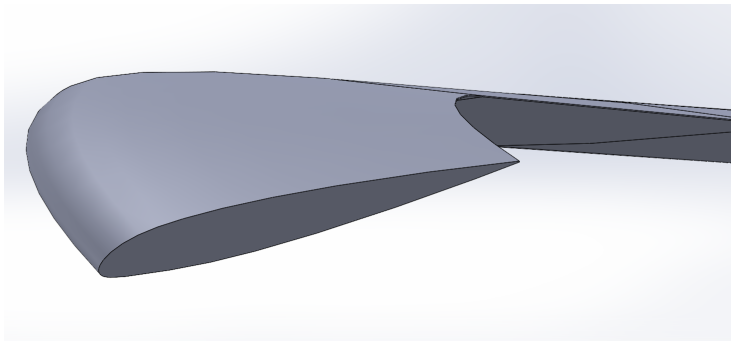

Figure 3.4: Particular of tip pitch down and anhedral

The start of the tip at 91% of the radius is referred to as the tip hinge. This is the tip rotation locus around which the anhedral angle is defined and will be changed during simulations; the hinge is a line that runs from leading to trailing edge. Moreover, a reference point is set at the feathering axis coordinate on the hinge line for moment evaluation; the rotation of the blade hinge around the reference point is defined by the angle ζ_{th}

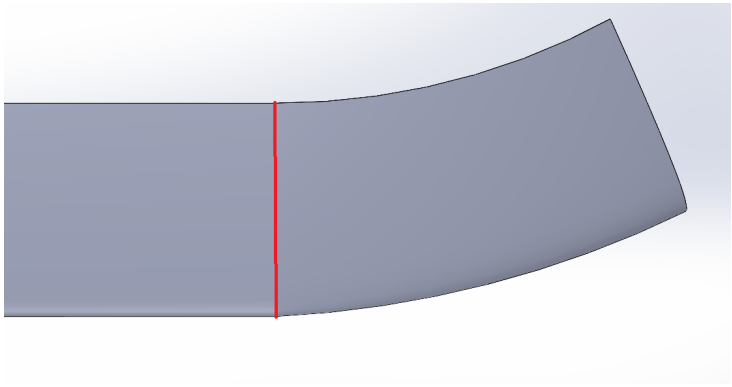

Figure 3.5: Particular of the hinge line

3.2. Rotor characteristics

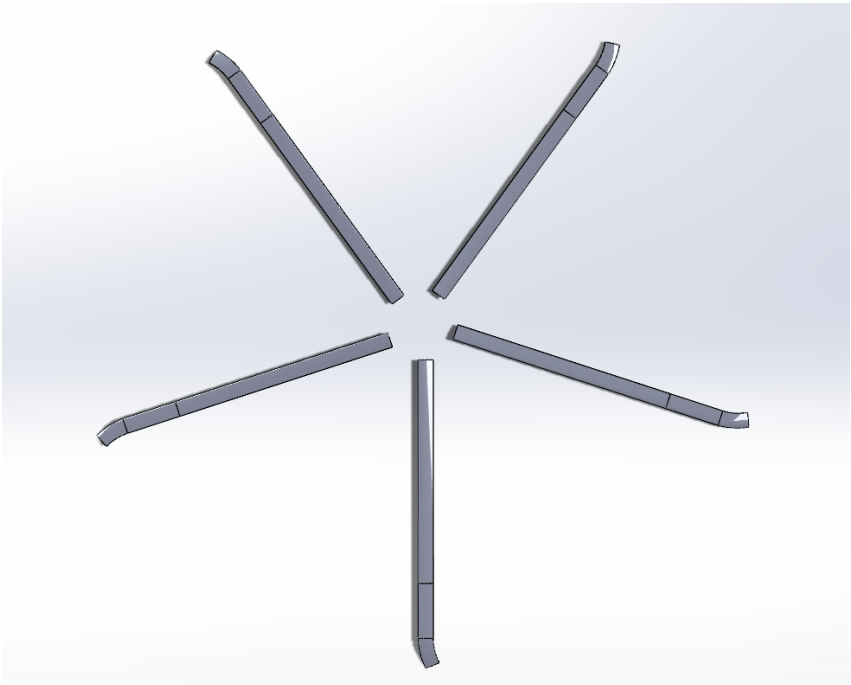

Figure 3.6: Rotor view from the top. Tip sweep is clearly visible

The whole rotor consists of 5 rotating blades. Thanks to the already discussed moving reference frame, the simulations will be computed in a steady environment with no time stepping. In order to reduce computational effort, a periodic boundary condition is introduced and only one of the blades will be actually simulated in the CFD solver.

The rotor and hovering characteristics are taken from Surra [20]. The required thrust was calculated from the helicopter maximum takeoff weight (MTOW). This piece of information was gained from manufactures websites. All pitch rotations are referred to the 75% of the blade radius, as it has null twist (θ_{75}).

Using the equation:

$$\Omega = \frac{M_{tip}\, a}{R} \tag{3.1}$$

where a is the speed of sound, it is possible to evaluate the blade tip mach number. As the rotor reaches 0.6, compressibility is taken into account. The solver uses an ideal gas law for air and standard atmospheric conditions as a reference. As already discussed in Chapter 1, inviscid Euler equations are used in the simulations. Although in a compressible condition, the speed is not high enough for any shock waves to form. This makes the meshing and simulation substantially easier and cheaper in computational cost.

MTOW	8200 Kg
Collective pitch θ_{75}	14°
Blades number	5
Thrust T	80221 N
Torque Q	63061 Nm
Coning angle β_0	6.94°
Rotating speed Ω	27.9763 rad/s
Mach number at blade tip	0.6

Table 3.2: Rotor characteristics

From these hovering reference values, it is possible to evaluate the coefficients from section 1.2, such that

$$\begin{cases} C_T = 9.4 \times 10^{-3} \\ C_Q = 1 \times 10^{-3} \end{cases}, \tag{3.2}$$

Consequently, the disk loading (DL) and Ideal Power Loading (PL) can be computed as well:

$$\begin{cases} \text{DL} = \frac{T}{A} = 479.174 \text{ N/m}^2 \\ \text{PL} = \sqrt{\frac{2\rho}{\text{DL}}} = 71.505 \text{ N/kW} \end{cases} \tag{3.3}$$

After having analyzed the hovering parameters, an overview of the rotor features and characteristics is necessary to understand all the simulations' settings.

3.2.1. Blade's hinge motion

A modern helicopter blade is capable of three different rotations during flight; the vertical flapping around the *flapping* angle β, the horizontal *lagging* and the *pitch* θ around the feathering axis.

The pitch angle is directly connected to the angle of attack of the blade and is carefully set by the pilot in order to maintain the helicopter in hover or any forward flight condition. Along with pitch, the flapping motion is taken into account and evaluated, while the lagging is neglected in this study as not considered to be relevant. This is due to the fact that this study focuses on a hover flight condition in a steady case. This setting would only present a small fixed value of lag angle that would not be relevant to loads' changes and therefore is neglected.

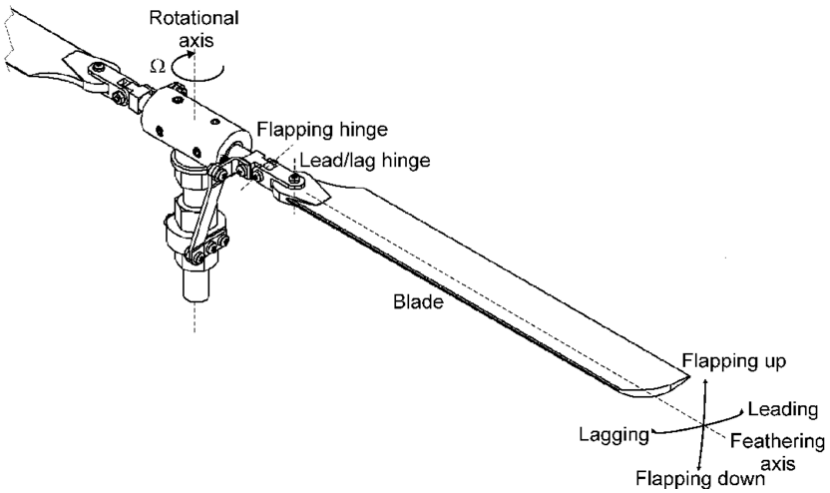

Figure 3.7: Blade hinge and its possible motions (Todorov, 2012 [12])

It is known that a bigger lift distribution is spread towards the outer region of the blade, generating a considerable flapping moment. This moment can wildly vary throughout different flight conditions, consequently creating a serious stress on the blade's root.

Any modern helicopter rotor presents a flapping hinge that nullifies any root bending moment of the blades, granting them to perform without stress loads in any flight condition. The hinge was developed and successfully applied by Juan de la Cierva in 1924 (Leishmann 2000 [9]) in order to nullify the rolling moment generated by fixed blades in forward flight. This hinge allows the blade to flap freely and so to increase the flapping angle due to the generated lift.

However, lift is not the only force acting on the blade; as it raises up, the centrifugal inertia force will create a flatting-out moment that opposes to the lift one. Eventually, the flapping angle of the blade will be the result of equilibrium between lift and inertia forces. In general, this equilibrium varies along the azimuth angle of the rotor, especially in forward flight; the mean value of the flapping angle on the rotor path is known as the *coning* angle β_0. Considering a hovering flight condition, the forces equilibrium will be steady and equal for all azimuth angles; therefore, the coning angle will be equal to the flapping angle and constant.

In the case of this study, the flapping hinge has an offset of 7% radius from the center. Given the fact that a CFD simulation utilizes a fixed geometry, the coning angle cannot be evaluated directly, as there is no way to account for inertia forces and free movement of parts. Therefore, the previous multi-body study analyses (Surra, [20]) were taken in consideration in order to obtain the value to set.

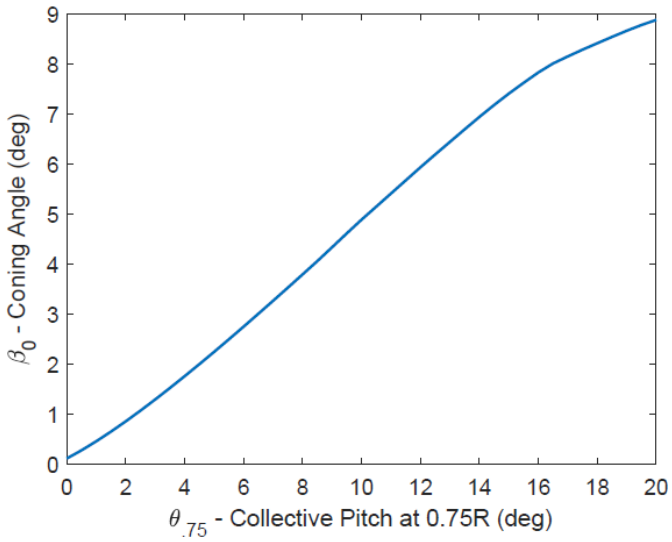

Figure 3.8: Coning angle variation

Figure 3.8 shows the data extrapolated from multi-body simulations. Naturally, the coning angle varies consistently with the increase of the pitch angle and consequently of the angle of attack of the blade. This data is related to the reference case of a 20° anhedral angle.

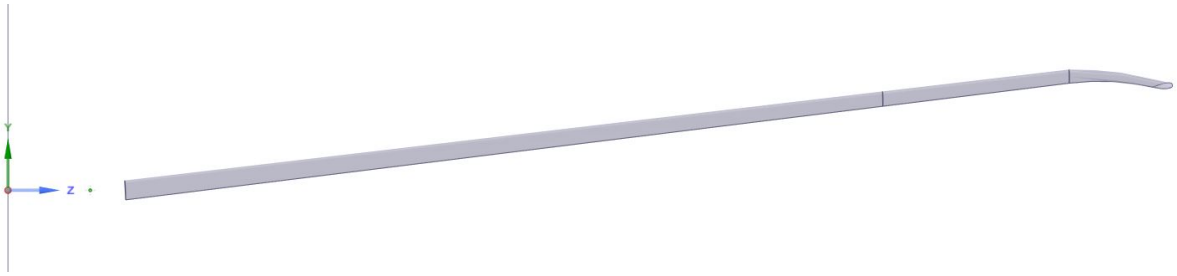

Figure 3.9: Evidence of coning angle

Figure 3.9 represents the geometry of a 14° θ_{75} simulation. The small green dot out of the Z axis is the flapping hinge center around which the blade is rotated. This elevation is considered and changed accordingly for every CFD simulation run in this study.

3.2.2. Inertia definition

The blade is designed with a strong use of composite materials. The study of Surra [20] focused on the choice of materials of three main parts: the spar, the core and the skin.

Although the CFD analysis does not focus on the structural composition of the blade,

the inertia effects were considered to be crucial in the behaviour of the rotor and of the effects on the tip. Therefore, external computations were done by assuming the mass of the blade as concentrated in two points: the centers of gravity of the rectangular section and the one of the blade's tip. All data was extrapolated from Surra's work, in which the author built a mesh model of the blade in Femap and computed all mass and inertial values.

Due to a difference in the reference frame used on the blade, the following transformations apply:

$$\begin{cases} x = -y_{surra} \\ y = z_{surra} \\ z = x_{surra} \end{cases} \tag{3.4}$$

Therefore, it is possible to compute all the data in the new reference frame.

	x_{cg}	y_{cg}	z_{cg}	M
Rectangular blade	−0.0114 m	0.0028 m	3.6648 m	47.5196 Kg
Blade's tip	0.0664 m	−0.036 m	6.448 m	2.7961 Kg
Overall blade	−0.007 m	0.0006 m	3.8471 m	50.3157 Kg

Table 3.3: Centers of gravity coordinates and masses

In table 3.3 the coordinates and masses of these points are reported. Specifically, the tip center of gravity will be crucial in order to calculate the inertial moment of the tip around its hinge.

Besides the point-wise masses, moments of inertia of the blade's parts were also considered as to take into account the spacial distribution of mass. Clearly, the relations 3.4 are used for translating the data into the new reference frame. Therefore, the inertia tensor components with respect to the center of mass are described in table 3.4.

[Kg m^2]	I_{xx}	I_{xy}	I_{xz}	I_{yy}	I_{yz}	I_{zz}
Rectangular blade	185.0474	−0.0072	2.3124	185.3773	−0.0421	0.3416
Blade's tip	17.5218	−0.0065	0.5754	17.5558	−0.0994	0.0437
Overall blade	230.9829	−0.0216	3.5615	231.3587	−0.4772	0.4052

Table 3.4: Moment of inertia components

The blade was rotated as a rigid body according to a set of pitch and anhedral angles. By knowing the original position of the tip center of mass and of the hinge, it was possible to evaluate the distance change between these points in all directions. These values are critical in order to calculate the moments generated by inertia forces.

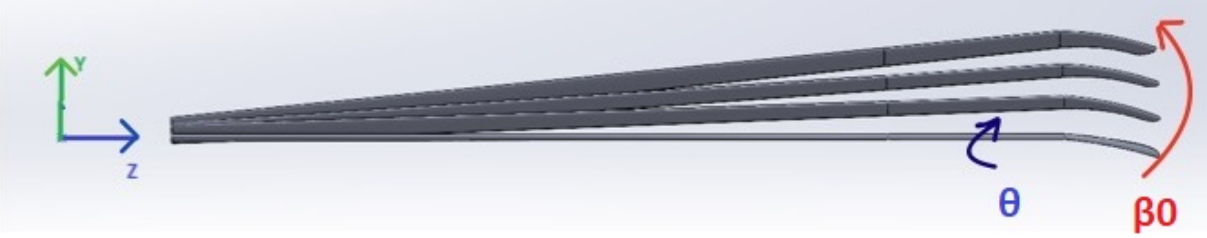

Figure 3.10: Various positions of the blade's rigid motion representation

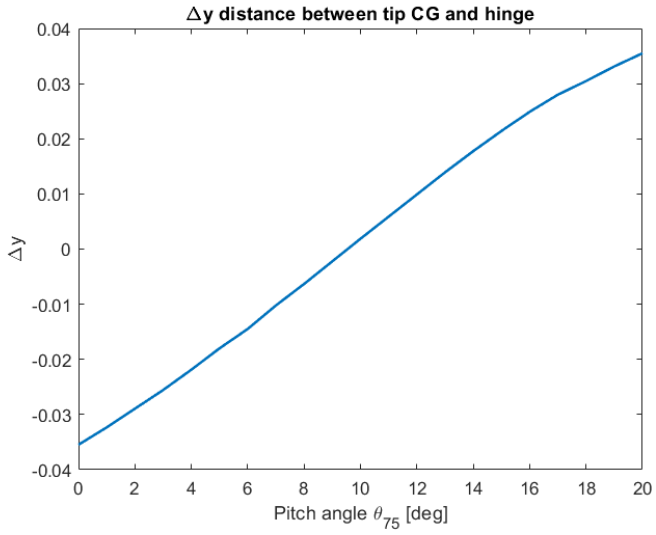

Figure 3.11: Vertical Δy distance for the standard blade

In figure 3.11 the vertical distance is displayed. This is considered to be the most important component of the three; it is interesting to note the change of sign at around 10° as it will be crucial later in the results.

The goal of this study is to focus on the blade's tip behaviour and on the possibility of an anhedral angle variation through loads. Therefore, the evaluation is focused on the overall moment around the tip hinge.

The moment given by inertia forces on the tip can be computed through a concentrated-mass approach. Let e be the hinge distance from the origin, R_{CG} the tip center of mass radius and ψ the anhedral angle of the tip center of mass

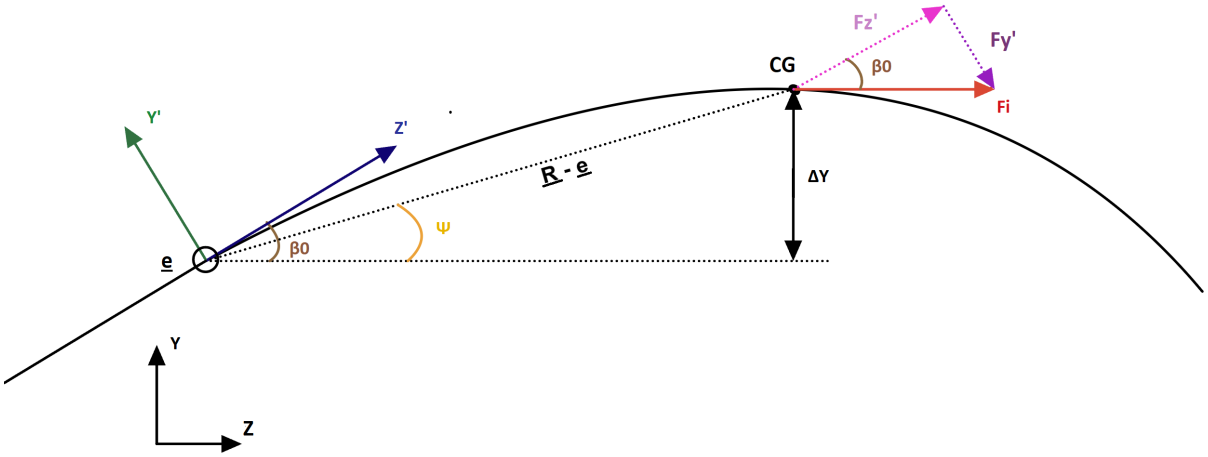

Figure 3.12: Schematic visualization of the blade tip angles (not to scale)

It is now possible to compute ψ through the Δy distance obtained earlier from rigid rotations.

$$\psi \approx \sin(\psi) = \frac{\Delta y}{|R_{CG} - e|} \tag{3.5}$$

Given the non-linear shape of the blade, ψ is not equal to the general tip anhedral angle β_{tip}, and it is only relevant for the tip center of mass.

The centrifugal force of equation $F_{in} = m\Omega^2 R_{CG}$ is considered to be horizontal due to the rotation of the blade around the vertical $\vec{y}$ axis. It is possible to define a local reference frame centered on the tip hinge and oriented as the inboard section of the blade; which is to say rotated as the coning angle β_0. In the new reference frame:

$$\begin{cases} F_{y'} = -F_{in} \sin \beta_0 \approx F_{in}\beta_0 \\ F_{z'} = F_{in} \cos \beta_0 \approx F_{in} \\ \Delta z' = |R_{CG} - e| \cos(\beta_0 - \psi) \approx |R_{CG} - e| \\ \Delta y' = -|R_{CG} - e| \sin(\beta_0 - \psi) \approx |R_{CG} - e|(\beta_0 - \psi) \end{cases} \tag{3.6}$$

Now, the moment given by inertia forces can be calculated around the tip hinge

$$M_{in} = F_{z'}\Delta y' - F_{y'}\Delta z' = F_{in}|R_{CG} - e|\psi \tag{3.7}$$

Equation 3.7 delivers the inertia moment generated by the concentrated mass in the tip CG. However, the model does not take into account the spatial distribution of the mass around the blade tip; this leads to a great loss of information.

The inertia moment equation can be formally solved by integrating a hypothetical distributed mass per unit length along the blade. Given that all angles are small, the blade is assumed to be parallel to just a single direction $d\vec{r}$

$$M_{in}^{distr} = \cancel{\int_e^R mr^2\,dr\;\ddot{\beta}_0} + \int_e^R mr\Omega^2(r-e)\psi\,dr \tag{3.8}$$

Equation 3.8 represents the inertial moment of the blade tip with respect to the hinge at position e. The $\ddot{\beta}_0$ acceleration term is missing as only the steady hovering case is considered; no dynamic flapping is present. Therefore, only the centrifugal force contributes to the moment that tends to flat-out the anhedral.

Expanding the term gives

$$M_{in}^{distr} = \left(\int_e^R mr^2\,dr \;-\int_e^R mr\,dr\;e\right)\psi\;\Omega^2 \tag{3.9}$$

We can now compute the integrals and find the contribution of the moment of inertia and the static moment

$$M_{in}^{distr} = I_{yy}^{CG}\;\Omega^2\;\psi - S_y^{CG}\;\Omega^2 e\;\psi \tag{3.10}$$

If we expand equation 3.7, we get:

$$M_{in} = mR_{CG}^2\;\Omega^2 - mR_{CG}\;\Omega^2\;e \tag{3.11}$$

By comparing equations 3.7 and 3.11, the terms look very similar to each other. However, the term $mR_{CG}^2\Omega^2$, although close in its formulation, is not the same as $I_{yy}^{CG}\;\Omega^2\psi$. Utilizing a strict concentrated mass approach leads to a loss of information; the spacial distribution of the mass around the tip contributes to the generation of a stronger inertia moment. Therefore it is necessary to add the moment of inertia component to the computation.

Eventually, following Surra [20], the centrifugal moment can be approximated to the sum of the concentrated mass term and of the moment of inertia.

$$M_{in}^{total} \approx F_{in}|R_{CG} - e|\psi + I_{yy}^{CG}\;\Omega^2\;\psi \tag{3.12}$$

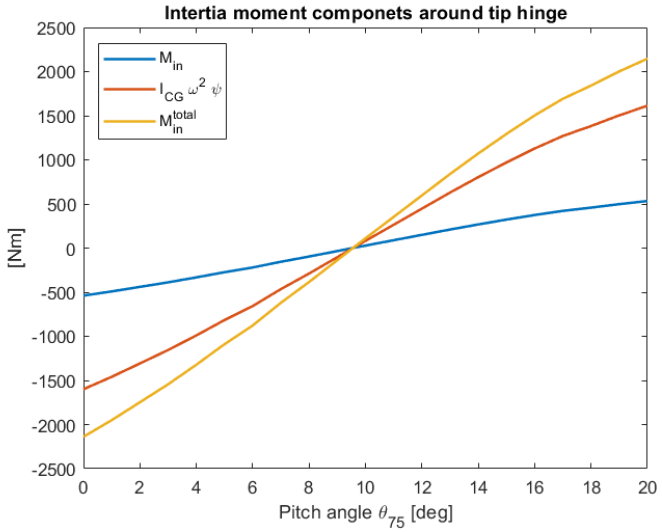

Figure 3.13: Inertia moment components

Figure 3.13 represents the two inertial components and the sum that is the total inertia moment acting on the blade hinge. As can be noticed, the moment changes sign at approximately $\theta_{75} = 9.55°$. This is due to the fact that the tip orientation crosses over or under the horizontal plane; as the inertia tends to *flat-out* the anhedral angle, the moment will switch sign accordingly.

3.3. Blade CFD simulation setup

The CFD domain is built by maintaining the same proportions as the Caradonna-Tung experiment. A $6R$ large cylindrical domain was created around the helicopter blade with a $1.5R$ inner rotating domain as shown in figure 3.14. The same periodic conditions of the validation are applied; being this a 5 bladed rotor, the periodicity angle is of 72°. The cell refinement on the blade is kept the same as the Caradonna-Tung one as the airfoils' chords dimensions are comparable. In the figure, the inner rotating domain is visible in the middle of the periodic wall.

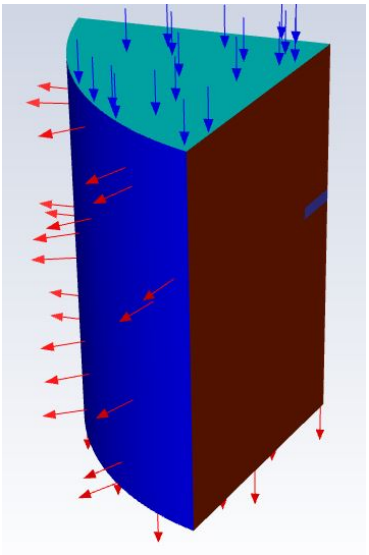

Figure 3.14: Blade CFD domain visualization

By using equation 1.4 and the data from table 3.2, the theoretical inlet velocity results in $v_{iM} = 13.985$ m/s. From there, the same experimental parameter computed in the model validation is applied using equation 2.6; the resulting inlet velocity is $v_i = 3.92$ m/s. This value, together with the pitch angle θ_{75} and the coning angle β_0, is modified in every simulation according to the expected thrust values computed by Surra [20].

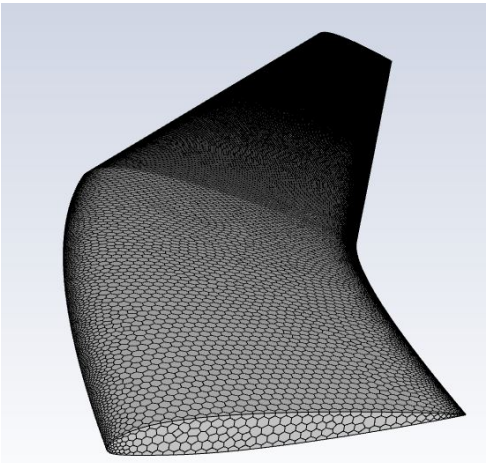

Figure 3.15: Blade mesh

Figure 3.15 represents a close up view of the blade tip and its mesh distribution. By using the same proportions of the *medium* mesh of the Caradonna-Tung validation, the mesh of the blade domain reached a size of 1.8 million elements.

The domain geometry building, the meshing process and the simulation setup were all done by scripting repetitive actions in Ansys. This way, it was possible to quickly analyze many different cases.

Operative conditions were set as standard, with a density of 1.225 kg/m^3 and a pressure of 101325 Pa.

Every simulation took approximately 1.5 hours to converge on a Intel i9 9900k 5.0 GHz processor and 32 GB of ram. Also, a Nvidia RTX 2070 Super graphic card was implemented to speed up the process thanks to the new GPU acceleration feature.

3.3.1. Pseudo-transient simulation

In order to further reduce computational time and expense, the simulation type for the blade was switched from stationary to pseudo-transient once convergence was assessed. Pseudo time-stepping, probably better known as pseudo-transient continuation, is an under-relaxation method. It consist of solving for the steady-state solution of time-evolving equations by setting an initial guess and using a time-stepper to evolve the solution forward. The pseudo-time step can be selected manually or be automatically computed by Ansys Fluent based on the characteristic length of the mesh model. The use of this method speeds up convergence dramatically, allowing the simulation to produce results in less than 1000 iterations.

4 | Results

In this chapter, results from CFD simulations are presented. Multiple sensitivity analyses were conducted with the goal of assessing the effectiveness of the anhedral angle and of the passive reconfiguration mechanism. The post-processing of data required the cross use of Ansys Fluent, Matlab and Paraview. The first two pieces of software were mainly used to extract solution data and plotting, while Paraview played a crucial role in the evaluation of tip loads.

4.1. Reference blade

The simulations run smoothly, obtaining a fast and steady convergence of the force values. The base reference case of 20° anhedral (β_{tip}), null hinge angle (ζ_{th}) and at 14° pitch (θ_{75}) is depicted in figure 4.1.

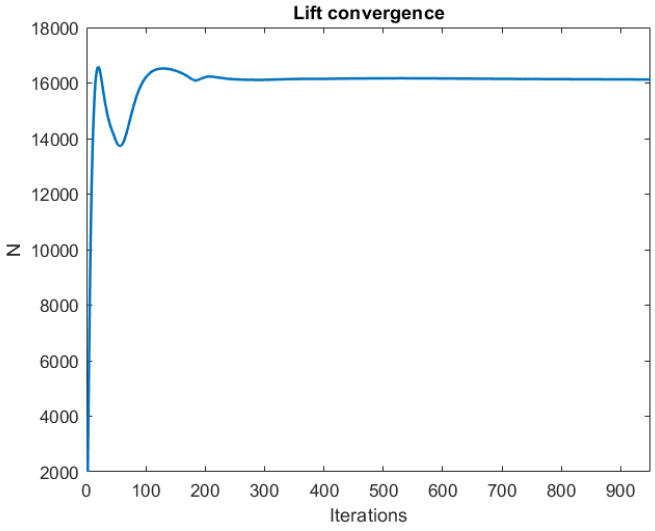

Figure 4.1: Reference blade lift convergence

Convergence was reached in a small number of iterations thanks to the use of the *COUPLED* scheme, pseudo-transient simulation and of the poly-exacore mesh (section 2.2.3).

Clearly, all the load values have to be multiplied by 5, as this is a single blade simulation with periodic boundaries. Following simulations showed the same behaviour and converged successfully in about 1000 iterations.

The reference blade at $\theta_{75} = 14°$ reached a generated thrust of 80625 N. Compared with an expected value of 80221 N from table 3.2, the simulation gives an error of 0.5%.

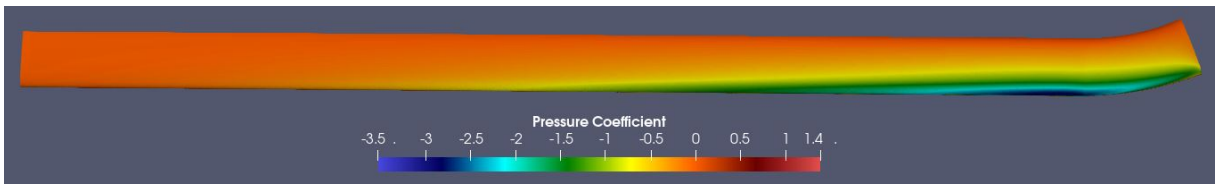

(a) Top view

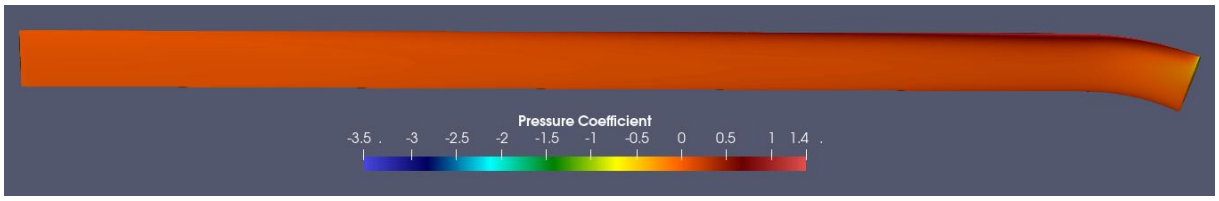

(b) Bottom view

Figure 4.2: Reference blade 0.8 R C_P distribution at $\theta_{75} = 14°$

Image 4.2 shows the pressure coefficient distribution with respect to the velocity computed at 0.8 R on the reference blade. As can be seen, the strongest suction happens to be slightly before the start of the tip, at around 0.85 R. The tip shape and orientation strongly influences this region and thus plays a crucial role in the thrust generation of the rotor.

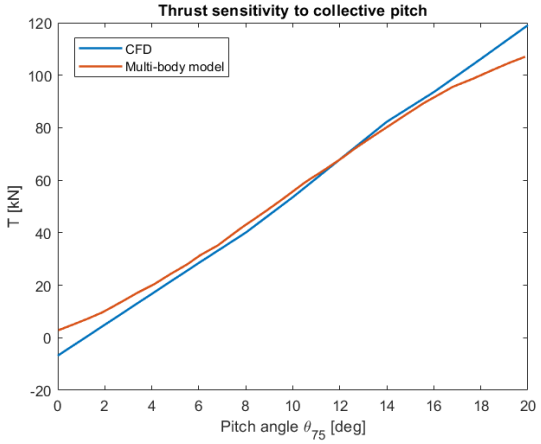

(a)

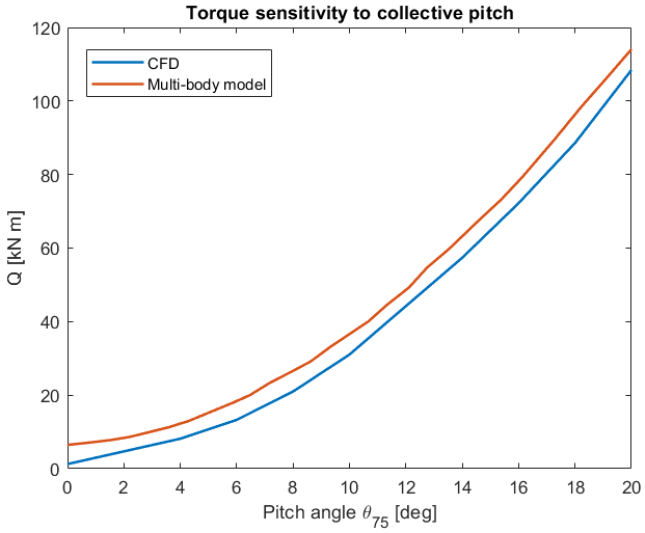

(b)

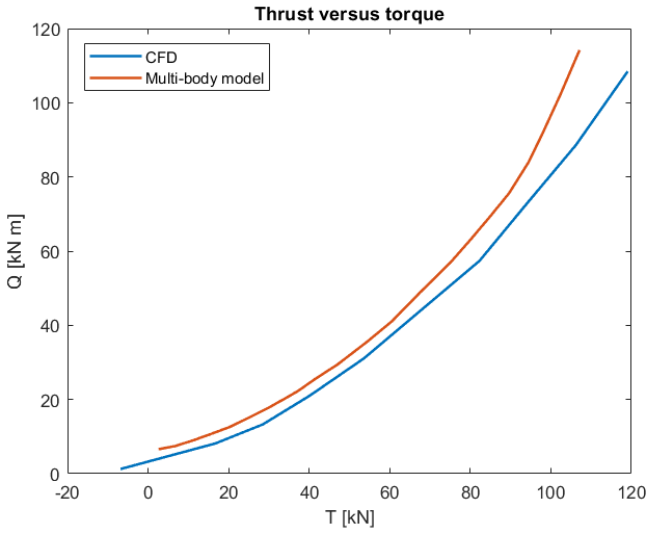

(c)

Figure 4.3: Rotor loads pitch sensitivity analysis

The blade was analyzed at varying collective pitch angle θ_{75} in a range from 0° to 20°, namely the operative scale. As expected, the thrust presents a linear behaviour as the blade is inside of the thin airfoil theory range. At zero collective pitch, the blade shows a slightly negative value for thrust (figure 4.3 (a)).

Results were compared with those obtained from the multi-body model [20], and appear to be very close to each other. The non-linear attitude of thrust is justified by the elastic movement of the rotor blades that is not replicated in the CFD simulations.

The torque evaluation relies on drag prediction, which is notoriously one of the weakest points of Euler equations based simulations and of CFD in general. The BEMT model utilized by Surra included loss coefficients and airfoil polars with viscous corrections in order to achieve a better solution. Because of this, the simulation's torque presents an absolute difference that remains steadily between 4.8 kNm and 6.52 kNm, as can be seen in figures 4.3 (b) and 4.4.

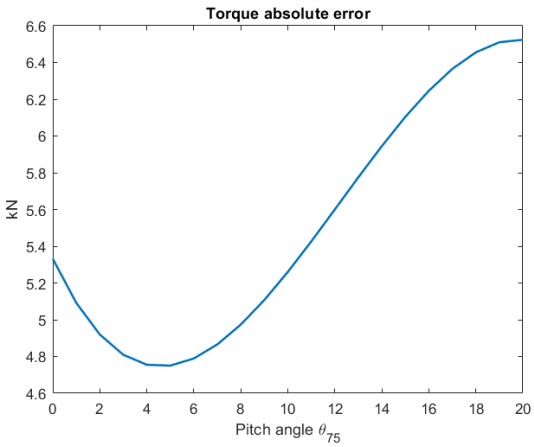

Figure 4.4: Torque absolute comparison

A further extension of the sensitivity analysis reveals that the blade enters the stall range at approximately $\theta_{75} = 26°$ with the formation of recirculation bubbles around the tip hinge region. Such a high stall angle is due to the use of the inviscid Euler method; it is known that the lack of viscosity and of the boundary layer keeps the flow attached to the blade at bigger angles of attack. However, as this thesis focuses on a normal operative range out of stall condition, this approximation is considered to be acceptable.

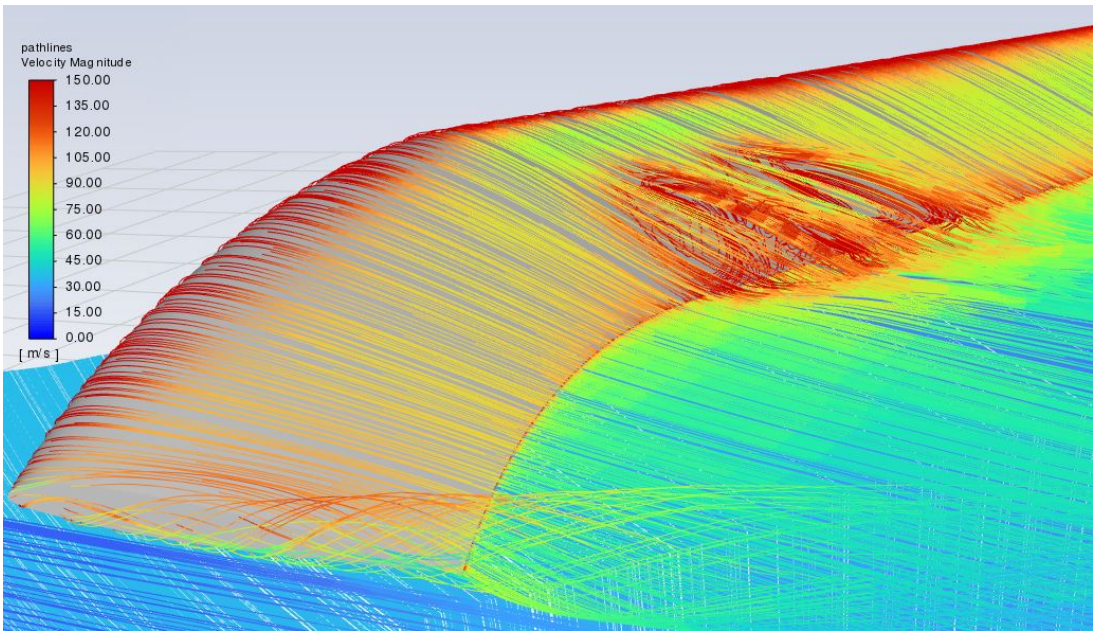

Figure 4.5: Streamlines view of blade tip at $\theta_{75} = 26°$

Figure 4.5 shows the recirculation bubbles and the flow detaching just before the tip hinge. The blade tip vortex is also visible.

4.2. Anhedral sensitivity

After assessing the blade's behaviour at various pitch angles, the tip anhedral was examined. Various configurations were investigated, ranging from the flat blade to a 40° β_{tip}. The hovering conditions were kept the same as the reference case, with a 14° collective pitch angle.

The hover figure of merit was computed at every configuration in order to have a better understanding of the rotor performance. The computational procedure is described by equation 1.5. The value for the reference case is FM=0.702, which is a number associated to a well designed rotor (Harris, 2017 [7]).

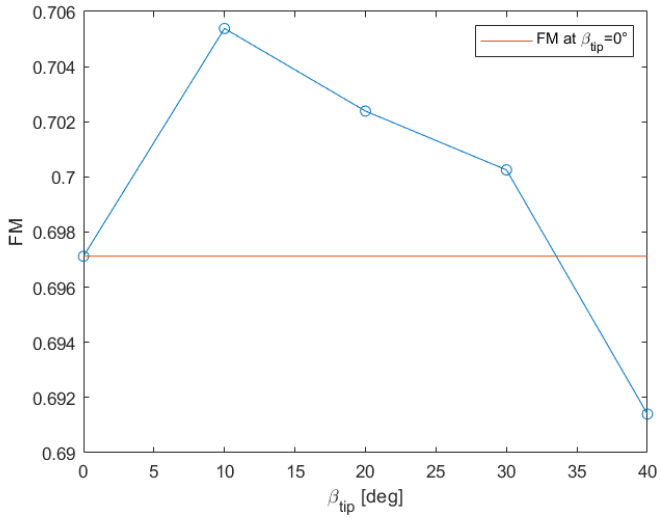

Figure 4.6: Figure of merit sensitivity to anhedral angle

The result of the evaluation is reported in figure 4.6; the red line represent the FM value of the flat blade (namely $\beta_{tip} = 0°$). As expected from the literature overview, the anhedral angle increases the hover figure of merit overall. Nevertheless, an excessive anhedral value of 40° will actually reduce the hover efficiency compared to a flat blade; this was also confirmed by literature, which usually suggest angles around 10° or 20°. In fact, for this particular blade the best condition is $\beta_{tip} = 10°$.

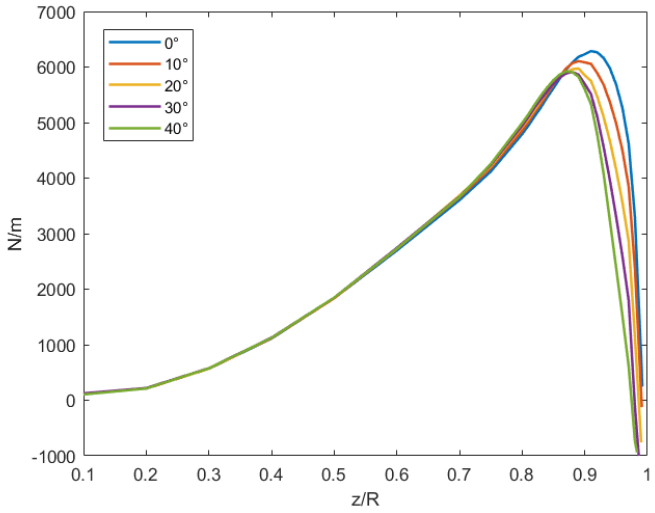

Figure 4.7: Lift distribution along blade span

The lift distribution was also investigated. As already seen in figure 4.2, the majority of thrust is produced at around 0.85 R with a sudden drop on the tip region. The increase of the anhedral angle causes the overall thrust value to diminish. The strongest difference happens between the flat blade and 20° anhedral, while the largest angles tend to maintain the same profile. The two last configurations are also related to a lower figure of merit as seen previously.

As the peak of lift lowers, so does the lift jump compared to the end of the tip. Because of Kelvin's theorem, all generated circulation is conserved and therefore leaves the blade at its end in the form of an extremity vortex. That being the case, a smaller difference of generated force translates in a smaller circulation value and thus in a weaker vortex shedding from the tip. Because of this, the drag value drops more compared to overall thrust and makes the drooped blade tip have a higher figure of merit during hovering.

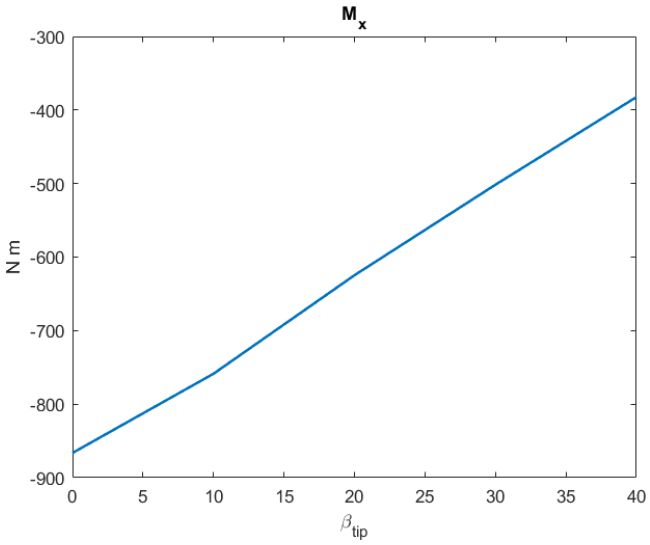

Figure 4.8: Tip moment anhedral sensitivity

Besides the overall blade, the tip region deserves particular attention as it is of upmost interest for this thesis. The moment evaluation with respect to the tip hinge reference point was computed at varying anhedral angles. Because of the reference system, the most interesting value is the moment around the $\vec{x}$ axis, which is collinear with the hinge axis and its positive value is associated with the anhedral reduction. Predictably, the aerodynamic force on the tip region produces a moment that tends to reduce β_{tip} due to the strong depression on the leading edge and lift generation (figure 4.9). Therefore, the computed aerodynamic moment is always negative and tends to reduce in modulus along the increase of the anhedral. This is coherent with the general thrust reduction seen previously.

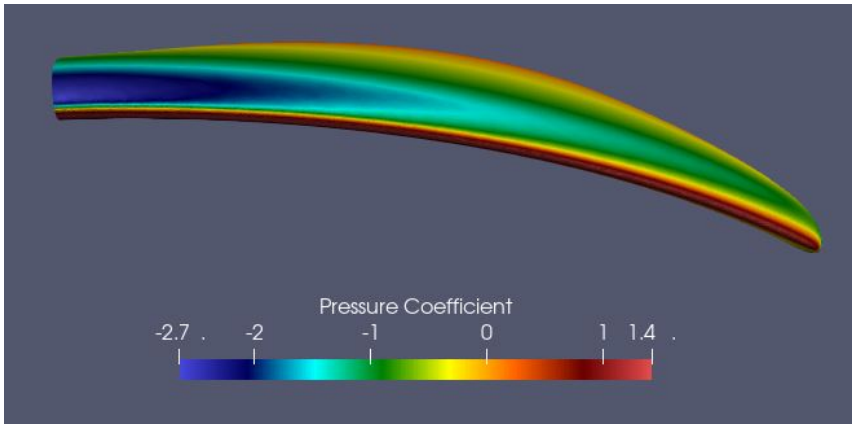

Figure 4.9: Pressure coefficient of the isolated tip region ($\beta_{tip} = 40°$)

4.3. Tip vortex analysis

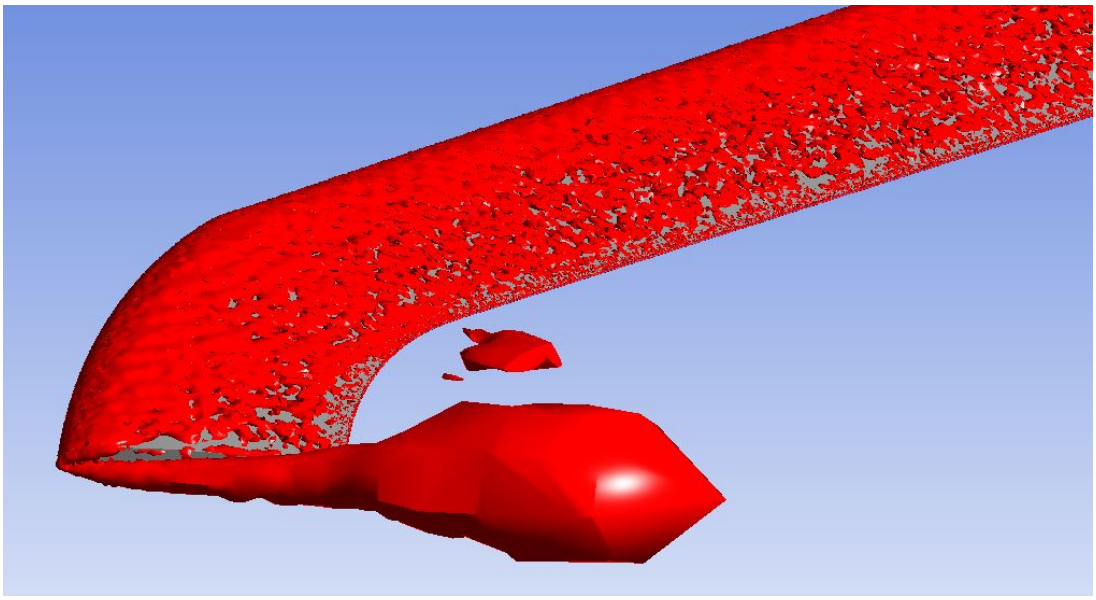

Figure 4.10: λ_2 criterion isosurfaces visualization of tip vortex

As previously stated, the presence of the anhedral angle of the tip lowers the thrust generated by the rotor along with the strength of the tip vortex, which in turn reduces drag. Besides having assessed the lift distribution, the blade extremity vortex was investigated in order to gauge its intensity at different anhedral angles and verify the effect. The vortex magnitude was regarded as the circulation of the flow in the vortex region, defined as

$$\Gamma = \oint_{\partial S} \vec{u} \cdot \mathrm{d}\vec{l} \tag{4.1}$$

Where ∂S is an arbitrary closed path around the vortex. This equation can be modified through the use of the Stokes' theorem into the flux of velocity's rotor, namely vorticity $\vec{\omega}$.

$$\Gamma = \oint_{\partial S} \vec{u} \cdot \mathrm{d}\vec{l} = \iint_{\Sigma} \nabla \times \vec{u} \cdot \mathrm{d}\Sigma = \iint_{\Sigma} \vec{\omega} \cdot \mathrm{d}\Sigma \tag{4.2}$$

This term can be approximated as a surface integral of vorticity on a flat surface, assuming that the vorticity field is always normal to the surface. To achieve this, a fictitious plane was chosen for the computation; it was placed at the origin with a 7° positive offset around the $\vec{y}$ axis, towards the rear of the blade. This surface was chosen arbitrarily to evaluate all blade configurations.

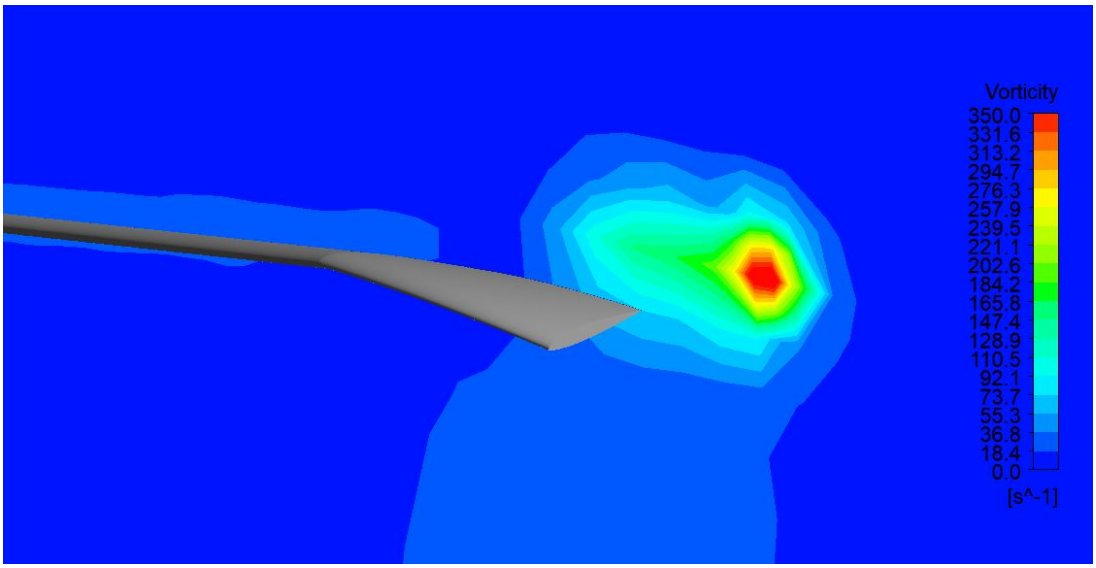

Figure 4.11: Vorticity evaluation on plane

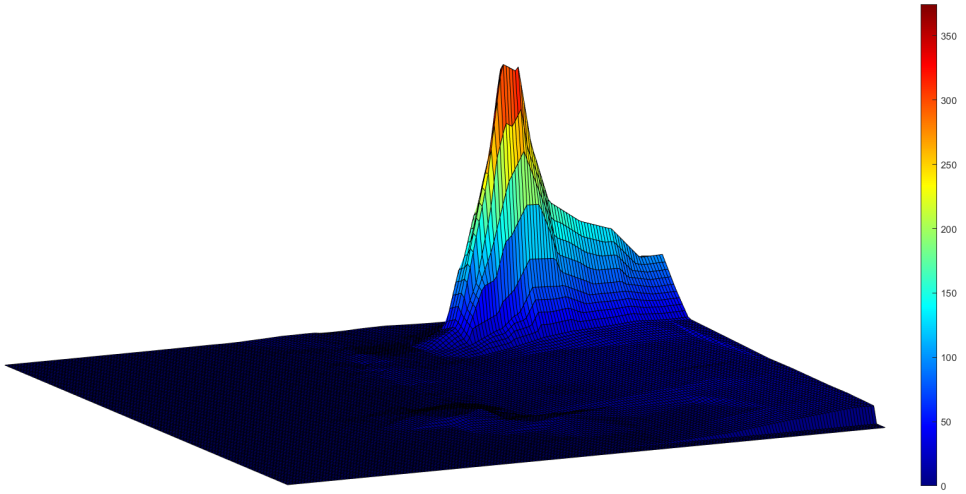

Figure 4.12: Vorticity peak on integration domain grid

The vorticity value was computed on this plane, which is right behind the blade tip as seen in figure 4.11. After that, a rectangular computational grid was built on the plane and used to determine the value of the surface integral to get the circulation. The area of integration was identified around the vorticity region of the tip vortex; given that values are all near zero with the exception of the vortex itself, the integration of the area can be considered equal to the integration of the vortex peak alone (figure 4.12).

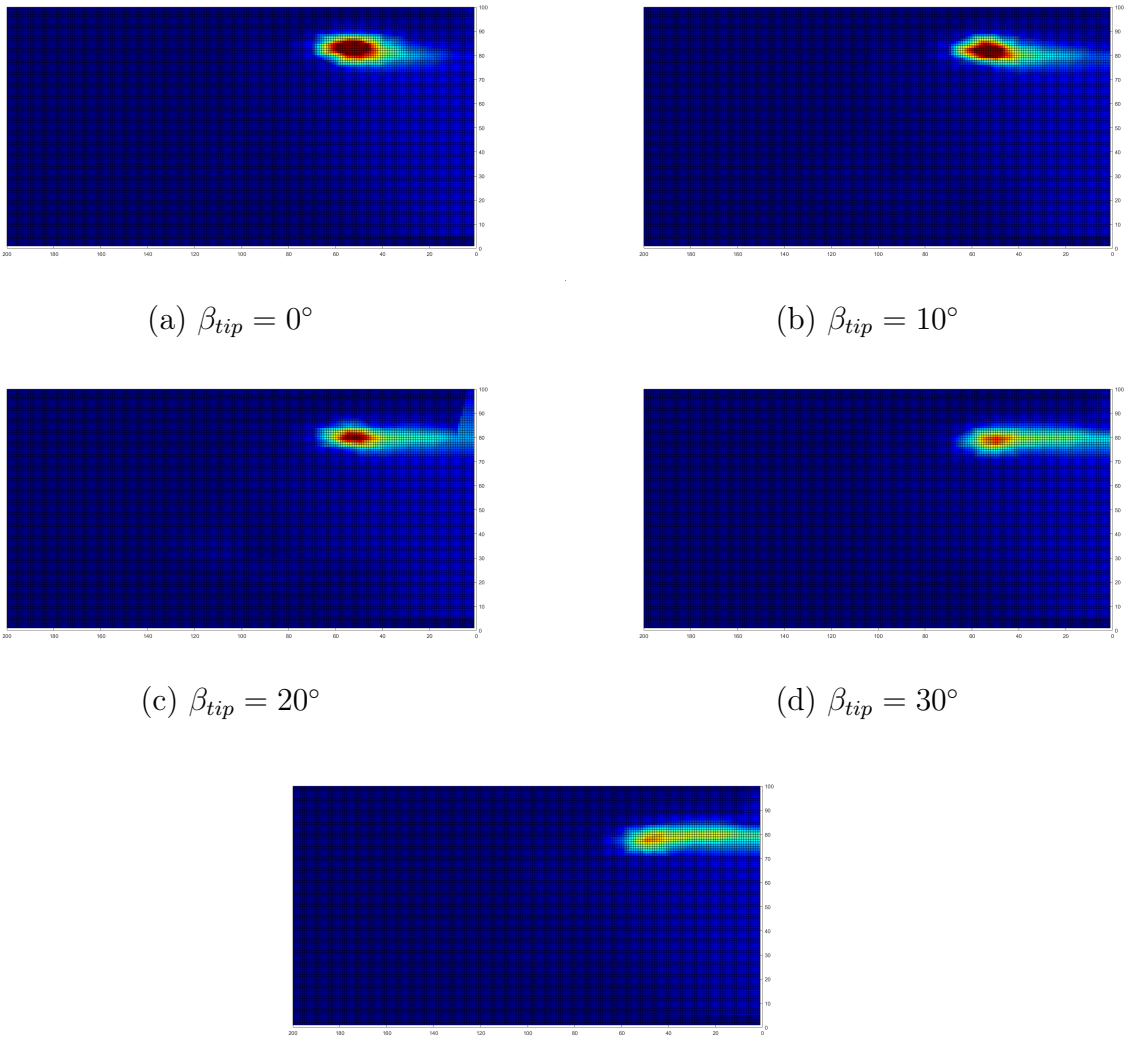

(a) $\beta_{tip} = 0°$

(b) $\beta_{tip} = 10°$

(c) $\beta_{tip} = 20°$

(d) $\beta_{tip} = 30°$

(e) $\beta_{tip} = 40°$

Figure 4.13: Tip region vorticity sensitivity to anhedral angle

The vorticity was evaluated at all anhedral angle configurations. As seen in figure 4.13, the increase of the droop makes the vortex core weaker and move downwards out of the rotor plane. This is an effective method to avoid blade-vortex interactions in hovering, but can have the opposite effect during forward flight in specific trim condtions. Besides becoming less intense, it is clear how the vortex deformes in the radial direction towards the inner side of the rotor (right side of pictures). This effect is particularly noticeable from 20° anhedral (figure 4.13 (c)) onward. As already discussed in chapter 1.2, the radial motion of vortexes towards the center along the increase of the anhedral angle is already widely observed in literature.

Once the domains had been extracted, the planar vorticity field was discretized in a computational grid of size 200x200. The circulation of each configuration was computed through numerical integration.

β_{tip}	Γ [m^2/s]
0°	86.083
10°	80.953
20°	78.08
30°	70.655
40°	70.397

Table 4.1: Vortex circulation sensitivity to anhedral angle

As expected, the vortex intensity lowers along the increase of the anhedral angle. The biggest jump is between 20° and 30°, after which the circulation value stabilizes. However, the 30° and 40° anhedral angles are not particularly relevant as they present various disadvantages in their implementation. First, as previously observed in figure 4.6, an excessive anhedral angle reduces the hover figure of merit and thus makes the tip geometry inefficient. Secondly, achieving large anhedral angles can be a great challenge on the structural point of view, rendering such a setup practically impossible.

4.4. Collective pitch sensitivity

After having assessed the behaviour of the tip and its components with the variation of the anhedral angle, the main analysis of the collective pitch is performed. A crucial part is the evaluation of the total hinge moment acting on the tip; the sign of this torque determines the possible reduction or increase of the anhedral angle. The reference blade with a fixed anhedral angle of $\beta_{tip} = 20°$ is used in the evaluation.

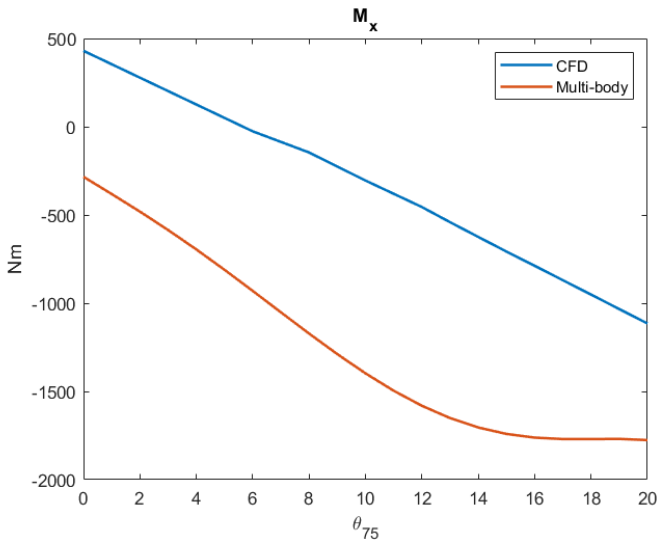

Figure 4.14: Aerodynamic tip hinge moment pitch sensitivity

Figure 4.14 shows the hinge torque extrapolated data from the CFD simulations and from the previous multi-body analysis by Surra. The BEMT based model predicts much stronger loads along all angles. The CFD data changes sign between 5° and 6° of pitch in an almost perferctly linear pattern. This is coherent with the thrust curve and in general with the linear aerodynamics range in which the blade operates. The flattening of the multi-body curve at high pitch angles is due to the elastic deformation and also to the approach of the stall region. As already stated in 4.1, the Euler inviscid method predicts the stall of the blade at a very high angle of attack, evidently higher than the real value. It is clearly noticeable that the three-dimensional CFD analysis predicts smaller aerodynamic loads on the tip region, resulting in less torque around the hinge.

The actual moment percieved by the tip hinge is the result of the sum between the one given by aerodynamic loads and the one generated by inertia forces. The total inertia moment was deeply discussed and evaluated in chapter 3.2.2, and presents a change of sign at approximately $\theta_{75} = 9.55°$.

Therefore, the total tip hinge moment is defined as:

$$M_{hinge} = M_{aero} + M_{in}^{total} \tag{4.3}$$

The curves are summed together, obtaining the final loads.

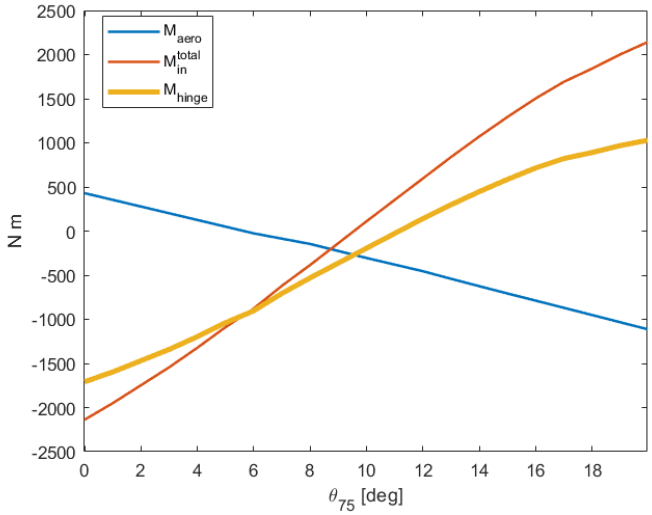

Figure 4.15: Total tip hinge moment pitch sensitivity

Figure 4.15 shows the two moment components and the final result of their joint action on the blade tip. The aerodynamic load lowers the value of the inertia term, shifting the zero-moment angle towards a higher value. A polynomial fitting interpolation of the curve revealed the zero moment angle to be approximately $\theta_{75}^{0} = 11.15°$.

This value is crucial as it determines the possible movement attitude of the blade tip. A collective pitch lower than θ_{75}^{0} will result in having a negative hinge moment on the tip; if the reconfigurable mechanism is released in this fragment, the sprag wheel will allow the tip to reduce its anhedral angle until reaching the desired value. Doing the same at a higher collective pitch than θ_{75}^{0} will result in an anhedral angle increase. It is interesting to note that, as shown in figure 4.8, the hinge moment anhedral sensitivity shows an opposite trend. Because of this, reducing the anhedral angle close to the flat blade configuration translates in an enlargement of the aerodynamic loads and therefore in an increase of the hinge moment. On the other hand, increasing the anhedral lowers the aerodynamic loads inducing less torque. This has to be taken into account in the design of the hinge system and its stiffness, as the tip will be subject to strong moment effects depending on the flight condition.

4.5. Hinge axis angle sensitivity

The design of the reconfigurable system allows the possibility of tilting the hinge axis of the tip. The movement is done around the hinge line reference point, located on the feathering axis at 20% of the section's chord c. This skew angle ζ_{th} is defined in a clockwise direction, with the hinge line reaching the tip rear during positive rotation.

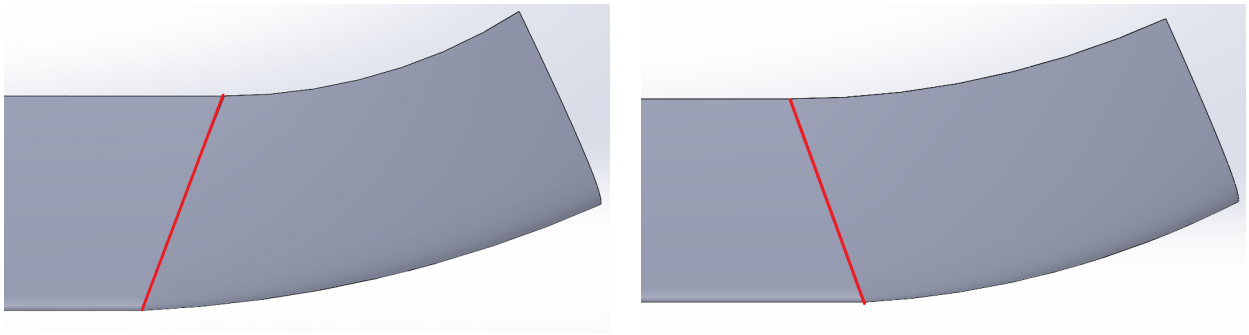

(a) $\zeta_{th} = 20°$ (b) $\zeta_{th} = -20°$

Figure 4.16: Tip hinge axis examples

Changing the hinge line orientation results in the deformation of the relative airfoil perceived by air impacting on the blade. Besides, the drooped tip presents a larger leading or trailing edge area depending on the angle sign. Eventually, 25 CFD simulations were carried out in order to analyze the effect of the hinge line rotation on hovering efficiency and on tip hinge moment. Every hinge configuration was studied by varying the anhedral angle at the reference hovering case of $\theta_{75} = 14°$.

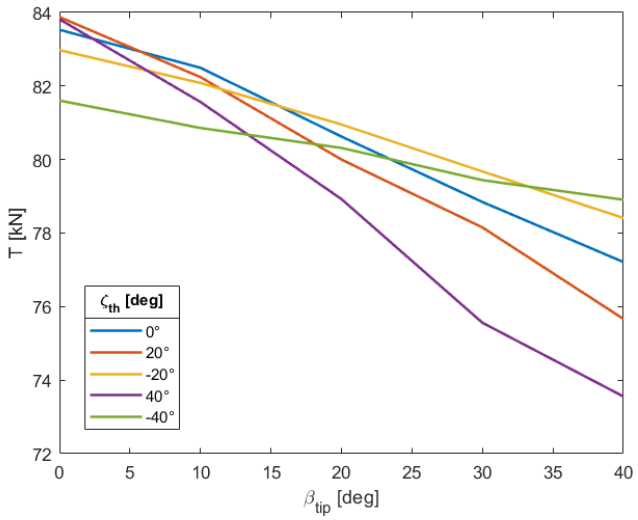

(a)

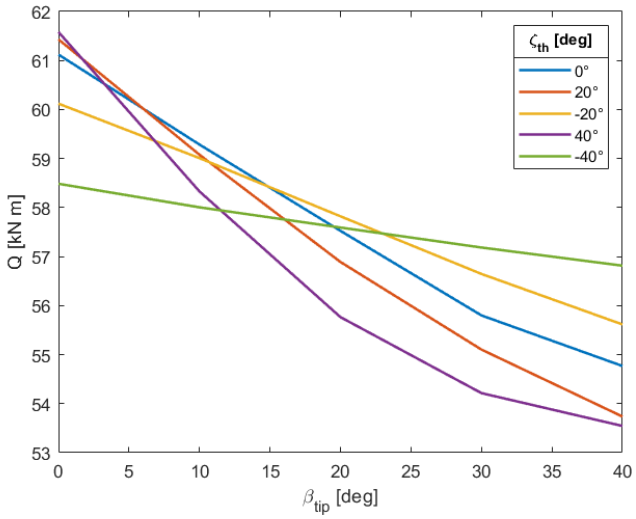

(b)

Figure 4.17: Rotor thrust and torque hinge angle sensitivity

The simulations' results showed a steady behaviour of the rotor in its configurations. Clearly, thrust and torque diminish along the increase of the anhedral angle, as previously assessed. In order to better appreciate the difference between the hinge axis settings, the hover figure of merit was computed for all configurations.

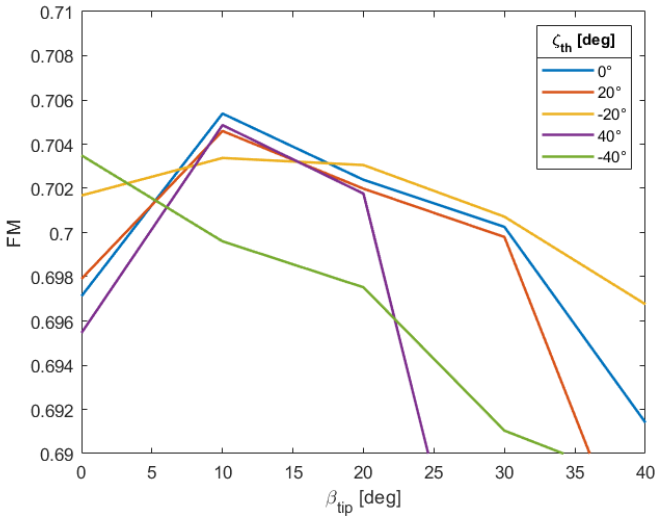

Figure 4.18: Hinge angle hover figure of merit

As seen in figure 4.18, most of the hinge line configurations reduce the hover efficiency compared to the reference blade case. Large angles deliver the worst results, with the $-40°$ case constantly reducing efficiency with respect to the flat blade. The $\zeta_{th} = -20°$ setting

is the only one to actually increase the figure of merit for anhedral angles higher than 20°, granting an improvement in this flight condition. This particular angle, although having a maximum figure of merit that is lower than the reference case, presents a more homogeneous efficiency across all anhedral distribution, with a higher efficiency also at $\beta_{tip} = 0°$.

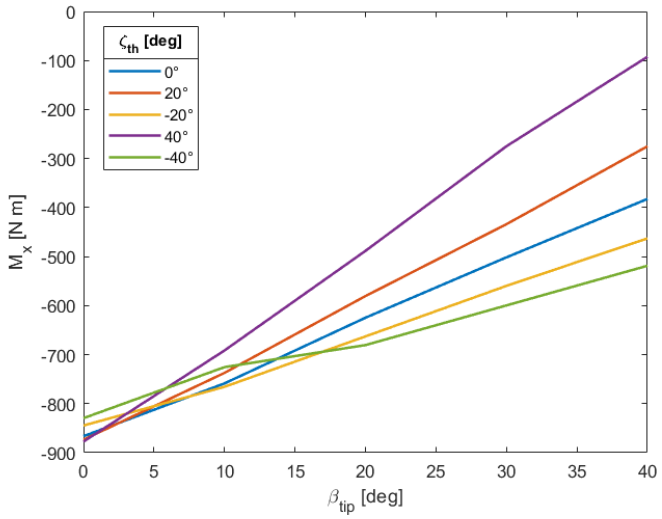

Figure 4.19: Hinge moment variation

Regarding the tip hinge moment, figure 4.19 shows an almost linear behaviour for all configurations. As expected, the moment value for the flat blade does not vary much across the hinge line angles. With the increase of the anhedral, positive hinge angles create a moment alleviation with respect to the reference case, while negative values make the moment modulus increase.

This aspect could be exploited in order to modify the null-moment pitch angle θ^0_{75} of the blade. Since the aerodynamic moment counteracts the action of the inertia moment, a stronger or weaker aerodynamic load will shift the null moment angle towards a higher or lower collective pitch depending on the hinge configuration. Typically, a higher pitch translates to a greater power required for flying, while a smaller angle could be exploited during a forward flight phase.

4.6. Tip center of pressure analysis

Following the hinge angle examination, the blade tip was further investigated by finding the location of the tip center of pressure. This way, the generation of the aerodynamic moment can be better understood. Achieving this is by no means easy and no such feature is present in most dedicated software.

The center of pressure can be defined as the locus where the summation of all aerodynamic generated moments is zero. Therefore:

$$\begin{cases} M_x = -F_y\, z + F_z\, y \\ M_y = F_x\, z - F_z\, x \\ M_z = -F_x\, y + F_y\, x \end{cases} \tag{4.4}$$

Ideally, by knowing the value of moments and forces on a certain region, one could compute the coordinates of the center of pressure. However, the set of equations 4.4 is not solvable on its own as it does not have a unique solution; all points along the line of action of a resultant force respect the zero moment condition. A constraint is needed in order to find a definite solution. Usually, CFD solvers allow the input of one of the three coordinates in space, practically defining a plane on which the center of pressure must be. However, given the strong three-dimensionality of the blade's geometry and its loads variation, this was considered not to be a good choice. A better educated guess is to constrain the center of pressure to be on a plane perpendicular to the total resultant force, namely:

$$F_x\, x + F_y\, y + F_z\, z = 0 \tag{4.5}$$

By inserting equation 4.5 into 4.4, the system is now solvable and finds the closest point to the origin of the reference frame that minimizes the total moment.

It is known that fluids generate pure couples on the bodies they act on, and these couples cannot take part in the computation of the center of pressure. Therefore, they have to be removed from the total moment evaluation. The pure couple $\vec{C}$ is identified as:

$$\vec{C} = \left(\vec{M} \cdot \vec{f}\right)\, \vec{f} \tag{4.6}$$

where $\vec{M}$ is the total moment vector and $\vec{f}$ is the unit vector in the direction of the total force. This component is then removed from the total moment and the equations can be

solved as:

$$\begin{cases} F_x\, x + F_y\, y + F_z\, z = 0 \\ M_y - C_y = F_x\, z - F_z\, x \\ M_z - C_z = -F_x\, y + F_y\, x \end{cases} \tag{4.7}$$

Resolving this system yields the point that minimizes the moment in any direction. This is the best approximation achievable for the center of pressure.

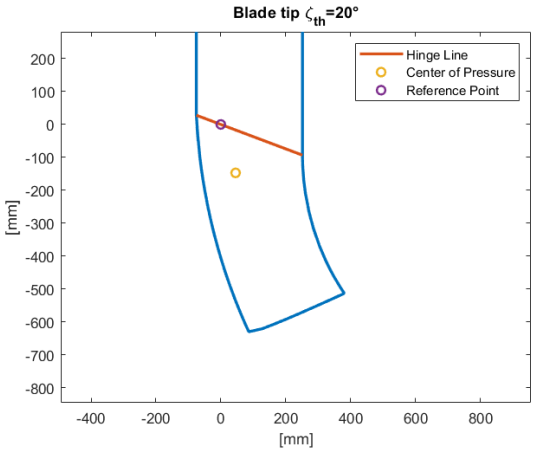

(a)

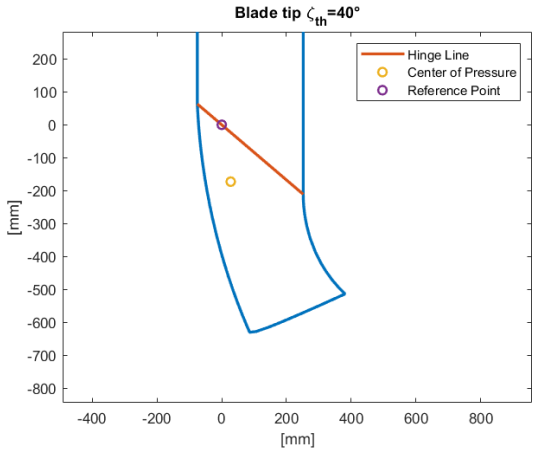

(b)

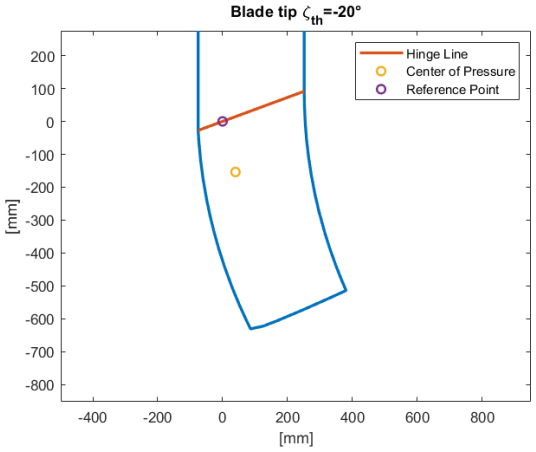

(c)

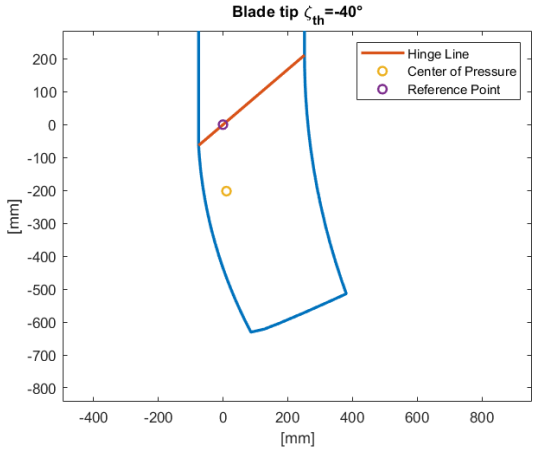

(d)

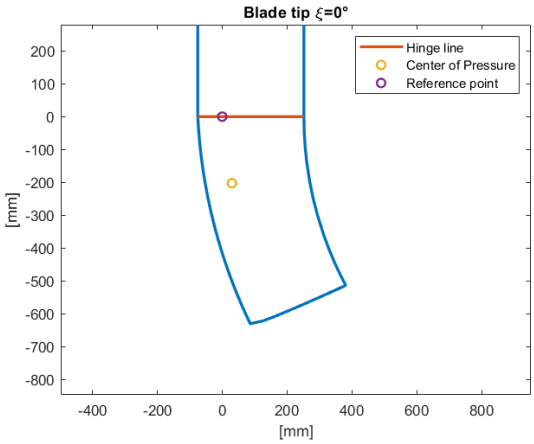

(e)

Figure 4.20: Blade tip center of pressure variation

Figures 4.20 show the different tip shapes and their hinge angle configurations, all in the reference condition of $\theta_{75} = 14°$ and $\beta_{tip} = 20°$. The reference point on the feathering axis is reported for clarity as the moments are evaluated with respect to it.

The center of pressure does not exhibit any large movements as the hinge angle changes, remaining close to the strongest depression zone of the blade. However, for negative hinge angles, the center of pressure tends to move towards the trailing edge and inward towards the hinge line; this can be appreciated in figures 4.20 (a) and (b), while the opposite effect can be noticed in figures (c) and (d). This behaviour relates to the moment trends seen in figure 4.19, where a positive hinge angle generates an alleviation of the loads. This is because the center of pressure moves closer to the hinge line and to the reference point of computation, actually reducing the moment arm. It could be possible that, for even higher values of ζ_{th}, the center of pressure would pass across the hinge line and deliver a moment of the opposite sign. Nevertheless, the use of extremely large angles is not advisable and remains extremely complicated on a structural point of view.

4.7. Passive actuation

After having gathered and analyzed all data, the best tip configuration for a passive actuation is investigated. First of all, CFD simulations of the blade demonstrate that the combination of inertia and aerodynamic moment can deliver an anhedral angle reduction with respect to the tip hinge. In order to achieve this condition, the overall moment value M_x has to be negative. As shown in figure 4.15, this happens with a collective pitch lower than $\theta_{75}^0 = 11.15°$.

As this thesis focuses on a hovering flight condition, it is known that the reference blade requires a collective pitch angle of $\theta_{75} = 14°$ in order to sustain the helicopters weight. For this value, the moment is positive and leads to an anhedral increase on the tip. However, it is possible to evaluate the data about forward flight from Surra's multi-body analysis. The complete rotor was simulated at various advancing ratios μ, defined as

$$\mu = \frac{V_\infty}{\Omega R} \tag{4.8}$$

where V_∞ is the helicopter movement velocity. Collective and cyclic pitch were computed iteratively in order to trim the rotor and to sustain flight.

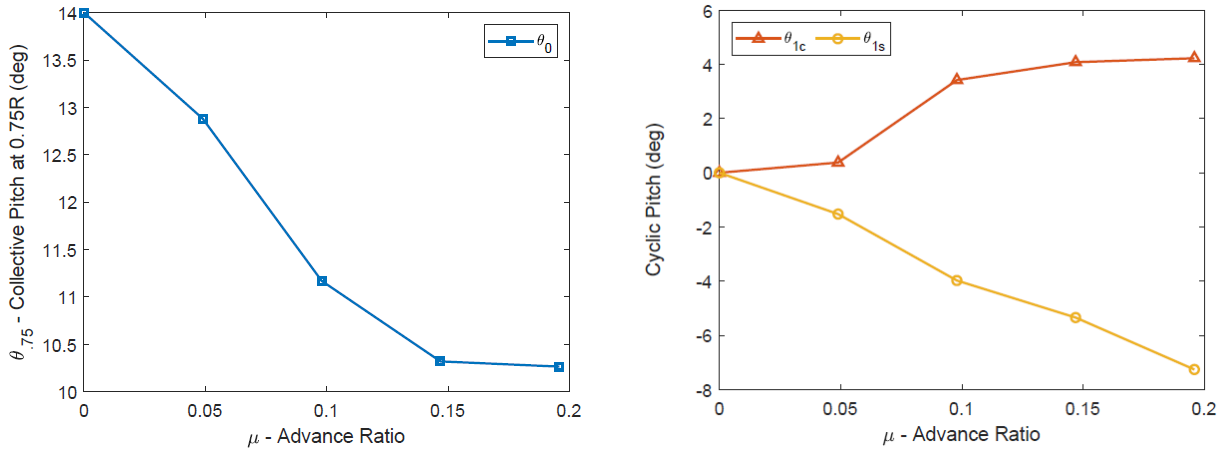

(a) (b)

Figure 4.21: Forward flight pitch trim values (Surra, 2019 [20])

From these analyses, it is clear that the value of θ_{75}^0 is easily reached and also passed during forward flight manoeuvres. Therefore, the anhedral reduction effect could be achieved outside of hovering for the reference blade with a base anhedral angle of $\beta_{tip} = 20°$. The mechanism could be manually released by the pilot in case of necessity.

Considering the reference blade, figure 4.19 shows that a skew hinge angle of $\zeta_{th} = -20°$ increases the hover figure of merit. Consequently, this configuration could be implemented for a better optimization of the flight condition. Besides, as seen in figure 4.19, the negative skew angle induces a higher aerodynamic moment, which translates to a slight increase of the tip null moment angle θ^0_{75}.

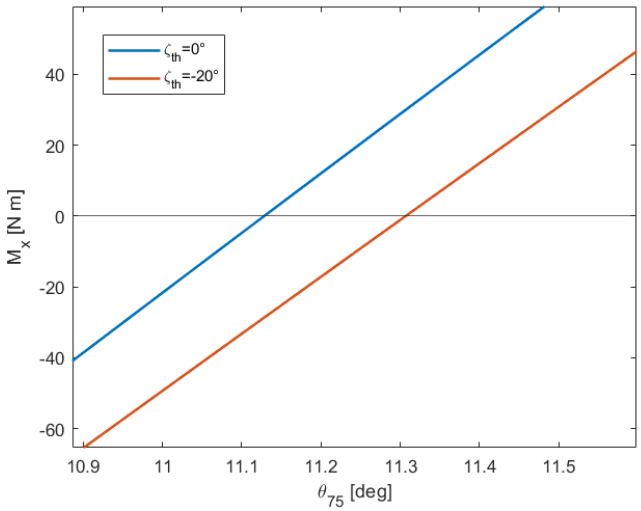

Figure 4.22: Null moment angle shift between hinge configurations

Computing the value in this new setting leads to a $\theta^0_{75} = 11.31°$, which is higher than the reference condition one but not in an appreciable way. Nevertheless, this $\zeta_{th} = -20°$ configuration is the best choice in terms of hovering efficiency.

Another option is to change the reference blade to one with a smaller value of anhedral angle. As seen in figure 4.18, a value of $\beta_{tip} = 10°$ delivers the highest figure of merit of all configurations. Therefore, adopting this anhedral angle as the base case would allow the rotor to fly as efficiently as possible. Also, a lower anhedral angle generates more thrust than required, thus a smaller collective pitch is required for hovering; this reduces the gap with the null tip moment angle.

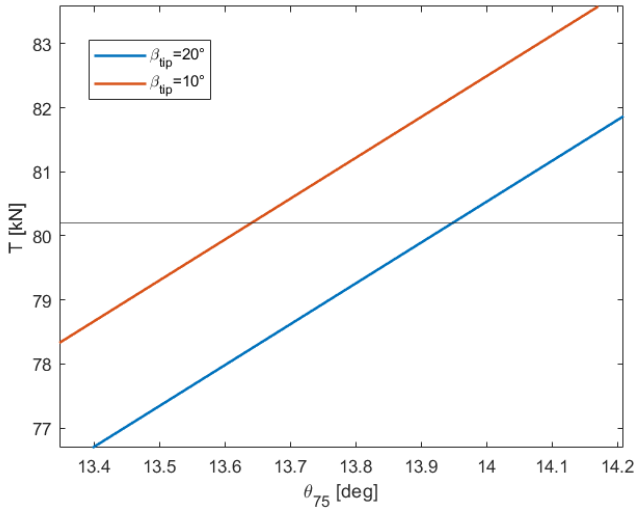

Figure 4.23: Hovering pitch angle shift shift between anhedral configurations

As seen in figure 4.23, the hovering pitch angle is reduced to $\theta_{75} = 13.62°$, slightly lower than the original value of 14°. This makes the null moment angle closer to the hovering collective pitch and easier to reach in forward flight manoeuvres.

5 | Conclusions and future developments

This thesis aimed at evaluating the feasibility of passive anehdral reduction on a blade's tip by exploiting the effects of aerodynamic and inertia loads. A CFD setup was validated and then used to analyze the blade in various configurations regarding hovering flight. In particular, the study focused on the variation of the tip's anhedral angle and on the hinge axis skew angle. After computing various CFD simulations, the tip hinge moment along with other parameters was investigated in order to understand if the passive actuation of the anhderal reduction would be possible.

The results show that, in order for the tip to experiment an anhderal reduction moment, the collective pitch angle has to be smaller than a certain treshold, which is lower than the design collective pitch required for hovering. Therefore, the study concludes that it is not possible to directly achieve an anhderal reduction during hovering flight. However, it was observed that, according to the previous multi-body study, the pitch threshold is reached and passed during forward flight. This opens the possibility to operate the reconfiguration mechanism and thus gives a positive response to the idea of a passive actuation system. Regarding the blade, two possible optimal configurations were found; the first presents a negative hinge skew angle of 20°, which increases hovering efficiency and also has a higher tip hinge moment, thus making the pitch threshold closer to the hovering condition. The second configuration consists of reducing the reference anhedral angle of the blade to 10°; this grants the best hovering efficiency of all setups and also allows to reduce the collective hovering pitch since the blade generates more thrust than needed. Both of these configurations need to be further analyzed as the power requirement prediction given by the CFD is not accurate enough to define them better with certainty.

As a prosecution of this study, the use of a viscous CFD model could improve the preciseness of the simulations by adding turbulence effects and a better drag prediciton. The use of a RANS model would require the construction of a more complex mesh, including special refinements around the blade for the boundary layer capture. Besides, the analysis

of a complete dynamic model would lead to more accurate results; a full aeroelastic model of the blade could be implemented with the coupling of the CFD solver with a structural solver. The blade's materials and component have already been defined and cleared in the multi-body study by Surra (2019, [20]). The study of the reconfiguration mechanism that allows the anhedral reduction also brings new possibilities; even though such systems exist in literature, the high rotational velocity and inertia forces of the blade render the design of these components extremely challenging.

Bibliography

[1] A. Meana-Fernández et al. "Application of Richardson extrapolation method to the CFD simulation of vertical-axis wind turbines and analysis of the flow field". In: *Engineering Applications of Computational Fluid Mechanics* (Mar. 2019).

[2] Foskey et al. *US Patent N.US20160075430*. Mar. 2016.

[3] *Ansys Fluent 2021 R2 User's Guide*. ANSYS Inc. Southpointe 2600 Ansys Drive Canonsburg, PA 15317, July 2021.

[4] C. Tung F. X. Caradonna. *Experimental and Analytical Studies of a Model Helicopter Rotor in Hover*. NASA, 1981.

[5] A. Brocklehurst G. Barakos. "A review of helicopter rotor blades tips shapes". In: *Progress in aerospace sciences* (Jan. 2013).

[6] Y. Mingchuan H. Shuilin F. Feng. *Aerodynamic Performance and Aeroacoustic Characteristics of Model Rotor with Anhedral Blade Tip in Hover*. JTrans. Nanjing Univ. Aero. Astro, 2018.

[7] F. D. Harris. *Hover Performance of Isolated Proprotors and Propellers—Experimental Data*. NASA Ames Research Center, Moffett Field, California, Dec. 2017.

[8] J. Salomon J. Ledoux S. Riffo. "Analysis of the Blade Element Momentum Theory". In: *SIAM Journal on Applied Mathematics* (July 2021).

[9] J. Gordon Leishman. *Principles of Helicopter Aerodynamics*. Cambridge University Press, 2000.

[10] E. Krämer M. Hollands M. Keßler. *Influence of an-/dihedral and of different blade shapes on performance and aeroacoustics of an isolated rotor*. IAG University of Stuttgart, Jan. 2012.

[11] A. Guardone M. Morelli T. Bellosta. "Development and preliminary assessment of the open-source CFD toolkit SU2 for rotorcraft flows". In: *Journal of Computational and Applied Mathematics* (2020).

[12] I. Dobrev et al. M. Todorov. "An investigation of the motion of a helicopter rotor with flapping and lead/lag hinges in hover". In: BulTrans-2012. Sozopol, Bulgaria, Sept. 2012.

[13] O. Szulc P. Doerffer. *Numerical Simulation of Model Helicopter Rotor in Hover*. Institute of Fluid-Flow Machinery PASa, July 2008.

[14] David R. Dowling P. K. Kundu I. M. Cohen. *Fluid Mechanics, 5th edition*. SG, Feb. 2012.

[15] A. Maligno et al. P. Marques. "The Jinn Military Unmanned Helicopter Program: Rotor Blade Tip Aerodynamics of the Advanced Technology Demonstrator". In: *International Journal of Unmanned Systems Engineering* (July 2013).

[16] R. Staufenbiel R. H. G. Muller. *The influence of winglets on rotor aerodynamics*. Vertica, 1686.

[17] J. P. Abraham S. Bhattacharyya. *Applications of Computational Fluid Dynamics Simulation and Modeling*. Suvanjan Bhattacharyya, Aug. 2021.

[18] W. Devenport S. Glegg. *Aeroacoustics of Low Mach Number Flows*. Academic press, 2017.

[19] O. Uzol S. Uluocak M. Perçin. "Experimental investigation of tip anhedral effects on the aerodynamics of a model helicopter rotor in hover". In: *Aerospace Science and Technology Volume 113* (June 2021).

[20] J. Surra. "Preliminary Investigation over a Reconfigurable Blade Tip for Rotors". MA thesis. Politecnico di Milano, Apr. 2019.

[21] E.N. Jacobs W. C. Clay. *Characteristics of the NACA 23012 Airfoil from Tests in the Full-Scale and Variable-Density Tunnels*. Technical report 530, 1935.

[22] K. Zore. "ANSYS Mosaic Poly-Hexcore Mesh For High-Lift Aircraft Configuration". In: 21st AeSI Annual CFD Symposium. Bangalore, India, Sept. 2019.